

AD-A279 417

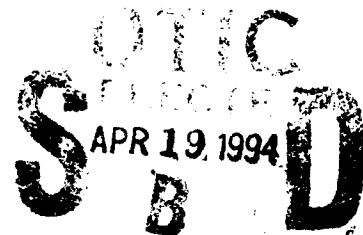


2

PL-TR-93-2168

DOPPLER WEATHER RADAR STUDIES OF PRECIPITATION SYSTEMS

F. Ian Harris
Teresa Bals
Ralph J. Donaldson
Donald Hamann
David J. Smalley



Hughes STX Corporation
109 Massachusetts Avenue
Lexington, MA 02173

December 1993

Final Report
May 1990 - May 1993

Original contains color
plates and photo reproductions
original is in black and
white

94-11728



APPROVED FOR PUBLIC RELEASE; DISTRIBUTION UNLIMITED.

REPRODUCTION PROHIBITED



PHILLIPS LABORATORY
Directorate of Geophysics
AIR FORCE MATERIEL COMMAND
HANSCOM AIR FORCE BASE, MA 01731-3010

94 4 18 13 9

This technical report has been reviewed and is approved for publication.



PAUL R. DESROCHERS
Contract Manager



DONALD A. CHISHOLM
Chief, Atmospheric Prediction Branch
Atmospheric Sciences Division



ROBERT A. McCLATCHEY
Director, Atmospheric Sciences Division

This document has been reviewed by the ESC Public Affairs Office (PA) and is releasable to the National Technical Information Service (NTIS).

Qualified requestors may obtain additional copies from the Defense Technical Information Center. All others should apply to the National Technical Information Service.

If your address has changed, or if you wish to be removed from the mailing list, or if the addressee is no longer employed by your organization, please notify PL/TSI, Hanscom AFB, MA 01731-3010. This will assist us in maintaining a current mailing list.

Do not return copies of this report unless contractual obligations or notices on a specific document requires that it be returned.

REPORT DOCUMENTATION PAGE			Form Approved OMB No. 0704-0188	
Public reporting burden for this collection of information is estimated to average 1 hour per response, including the time for reviewing instructions, searching existing data sources, gathering and maintaining the data needed, and completing and reviewing the collection of information. Send comments regarding this burden estimate or any other aspect of this collection of information, including suggestions for reducing this burden, to Washington Headquarters Services, Directorate for Information Operations and Reports, 1215 Jefferson Davis Highway, Suite 1204, Arlington, VA 22202-4302, and to the Office of Management and Budget, Paperwork Reduction Project (0704-0188), Washington, DC 20503.				
1. AGENCY USE ONLY (Leave blank)	2. REPORT DATE December 1993	3. REPORT TYPE AND DATES COVERED Final (May 1990 - May 1993)		
4. TITLE AND SUBTITLE DOPPLER WEATHER RADAR STUDIES OF PRECIPITATION SYSTEMS		5. FUNDING NUMBERS F19628-90-C-0088 PE63707F PR2781 TA01 WUAF		
6. AUTHOR(S) F. Ian Harris, Teresa Bals, Ralph J. Donaldson, Donald Hamann, and David J. Smalley				
7. PERFORMING ORGANIZATION NAME(S) AND ADDRESS(ES) Hughes STX Corporation 109 Massachusetts Avenue Lexington, MA 02173		8. PERFORMING ORGANIZATION REPORT NUMBER Hughes STX Scientific Report #8		
9. SPONSORING / MONITORING AGENCY NAME(S) AND ADDRESS(ES) Phillips Laboratory 29 Randolph Road Hanscom AFB, MA 01731-3010 Contract Manager: Paul R. Desrochers/GPAP		10. SPONSORING / MONITORING AGENCY REPORT NUMBER PL-TR-93-2168		
11. SUPPLEMENTARY NOTES				
12a. DISTRIBUTION / AVAILABILITY STATEMENT Approved for public release; distribution unlimited			12b. DISTRIBUTION CODE	
13. ABSTRACT (Maximum 200 words) Research under this contract was directed toward the development of new techniques to monitor and forecast the behavior of precipitation systems with Doppler weather radar. Focus was on the characterization of precipitation fields and of associated wind fields. Particular aspects that were examined are precipitation location, motion and type, synoptic scale and gust fronts, and the characterization of hurricane physical and kinematic structure. All analysis and forecast techniques are appropriate for a real-time operational environment. In addition, research has been completed toward the archiving and analysis of data from a wind profiling radar system. Efforts involved the definition of management, quality control, transformation, perusal, and extraction techniques for the profiler data. Also, techniques were developed to evaluate the meteorological conditions contributing to observed differences between the Loransonde and profiler wind estimates.				
14. SUBJECT TERMS Doppler weather radar, automated techniques, wind profiler, hurricanes, precipitation, freezing rain detection, front detection, gradient computation			15. NUMBER OF PAGES 68	
			16. PRICE CODE	
17. SECURITY CLASSIFICATION OF REPORT Unclassified	18. SECURITY CLASSIFICATION OF THIS PAGE Unclassified	19. SECURITY CLASSIFICATION OF ABSTRACT Unclassified	20. LIMITATION OF ABSTRACT Unlimited	

TABLE OF CONTENTS

1. INTRODUCTION	1
2. VAD ANALYSIS	1
2.1. Define VAD Analyses	1
2.2. Describe Processing	3
3. GRADIENT DETECTION	3
4. FRONT DETECTION	5
5. PRECIPITATION LOCATION/MOTION DETERMINATION	11
5.1. Introduction	11
5.2. Detection Techniques	12
5.2.1. Contour Extraction.	13
5.2.2. Edge Extraction	14
5.2.3. Feature Detection	14
5.3. Tracking Technique	15
5.4. Forecasting Techniques	19
5.5. Conclusions	20
6. PRECIPITATION TYPE ESTIMATION	22
6.1. Introduction	22
6.2. Algorithm Definition	22
6.2.1. Precipitation Phase Detection	22
6.2.2. Freezing Rain Detection	24
6.3. Future Considerations	26
6.4. Conclusion	26

7. HURRICANE LOCATION DETERMINATION	27
7.1. Introduction	27
7.2. Technique	28
7.3. Analysis	29
7.4. Summary	34
8. HURRICANE INTENSITY ESTIMATION	37
8.1. Potential Vortex Fit	37
8.2. Radial Confluence Index	39
8.3. VAD Analysis Applied to Hurricane Assessment	50
8.3.1. VAD-Derived Wind Parameters	51
8.3.2. VAD Perturbation Wind Field	55
8.3.3. Conclusions	55
9. WIND PROFILER EVALUATION	57
9.1. Introduction	57
9.2. Study Description	58
10. REFERENCES	63

Accession For	
NTIS GRA&I	<input checked="" type="checkbox"/>
DTIC TAB	<input type="checkbox"/>
Unannounced	<input type="checkbox"/>
Justification	
By	
Distribution/	
Availability Codes	
Dist	Avail and/or Special
A-1	

1. Introduction

Efforts under this contract have been to develop techniques that will assimilate data into usable products for the operational forecaster. Focus has been in several different areas: precipitation characterization, hurricane assessment, and wind profiler evaluation. In all of these areas, Doppler weather radar has been the primary observational tool. In the first two, conventional scanning Doppler systems, like the WSR-88D Next Generation Weather Radar, were used. In the latter, a new vertically pointing Doppler radar, commonly referred to as a wind profiler, was utilized.

2. VAD Analysis

2.1. Define VAD Analyses

Doppler radar has the capability of measuring a component of the motion of the scatterers at discrete range intervals of the order of 1 km or less over ranges from near 0 to 100 km or more. Because the measured component is directed along the beam, the radar measures a differing component of the motion as the beam changes its orientation in azimuth or elevation. The resultant measurements are best expressed in spherical coordinates, where the relationship between the three-dimensional motion and the radar radial velocity (V_r) is given by:

$$V_r(\beta, \theta) = u \sin(\beta) \cos(\theta) + v \cos(\beta) \cos(\theta) + w \sin(\theta) \quad (1)$$

where β and θ are azimuth (measured relative to north) and elevation angles for the radar beam and u , v , and w are the three rectangular Cartesian components of the motion. This is basically one equation with three unknowns. However, by fitting an equation of the form of the above expression to data collected around a complete circle, it is possible to extract estimates of u , v , and w . To solve for the motion values with the equation in this form involves invoking the assumption that these components are invariant around the VAD circle. This, unfortunately, is not a valid assumption and can produce very large errors. If one then expands the above expression to higher harmonics and allows the individual components to vary linearly across the domain, the components can be expanded in terms of their first order derivatives. This yields an expression of the form:

$$\begin{aligned} V_r(\beta, \theta) = & \frac{r}{2} \left(\frac{\partial u}{\partial x} + \frac{\partial v}{\partial y} \right) \cos^2 \theta + w \sin \theta \\ & + \left(u_o + \frac{\partial w}{\partial x} r \sin \theta \right) \sin \beta \cos \theta + \left(v_o + \frac{\partial w}{\partial y} r \sin \theta \right) \cos \beta \cos \theta \\ & + \frac{r}{2} \left(\frac{\partial v}{\partial x} + \frac{\partial u}{\partial y} \right) \sin 2\beta \cos^2 \theta + \frac{r}{2} \left(\frac{\partial v}{\partial y} - \frac{\partial u}{\partial x} \right) \cos 2\beta \cos^2 \theta \\ & + \text{higher order terms} \end{aligned} \quad (2)$$

The terms u_o and v_o are the velocity components at the radar ($r=0$). If the elevation angle is kept small, this equation can then be used to derive the characteristics of the horizontal motions such as mean velocity, divergence, and shearing and stretching deformation.

2.2. Describe Processing

Two techniques have been widely used to extract the wind velocities from the radar data: *harmonic analysis and least-square-fit of a multi-harmonic sinusoid curve* to the data. The former is a simplification of the latter when the data cover a complete circle (0 to 360°) at uniform intervals with no gaps. Our studies have shown that if harmonic analyses are applied to non-uniformly spaced data, significant errors can result. The least-squares-fit approach is far less restrictive in that the data do not need to be regularly spaced and they do not need to *encompass a complete circle*. However, any data gaps must be less than about 30° for reliable estimates to be derived. For all analyses presented in this report, the least-squares-fit approach has been used.

3. Gradient Detection

In meteorology, much of our feature identification in data relies on pattern recognition. Our eyes tend to key on gradients as delimiters as much as or perhaps even more than on extrema. Under this contract, we developed a technique for the extraction of gradients and have applied this technique to several tasks. In this section we will briefly discuss this technique.

Since radar data have been commonly evaluated in terms of what is seen visually on screens, it followed naturally that the task might instead be viewed as an imaging problem. Work in computer vision has already solved many image analysis problems in such areas as robotics, medicine and astronomy. A major tool used in these areas is the detection of edges of objects and subsequently characterizing these

objects by these edges. It is this ability that we have exploited for the detection of fronts. Here, we will only present a brief overview of this effort and refer the reader to two previous reports -- Hamann (1991) and Hamann (1992) -- for more detail.

An integral part of the technique is the computation of fields of gradients. This is most efficiently done through the application of templates. As will be seen, this approach will yield estimates of the magnitude and direction of the local two-dimensional gradient. Through an iterative process outlined below, lines joining maxima in the magnitude fields are constructed. These resultant lines, therefore, define the edge or boundary of a feature (e.g. gust front, or precipitation area) in the data field.

The first step in the processing is the interpolation to rectangular Cartesian space of the data that were collected within a spherical coordinate framework. Two techniques have been used: bilinear three-dimensional interpolation and a nearest point placement. The first is slower but much more predictable in its behavior than the latter because it uses well-defined interpolation formulae. Nearest point placement simply accepts the data point nearest to the grid point. This latter technique produces excellent results in close to the radar, but at distances where the data azimuth/elevation resolution is greater than the grid spacing, artifacts are produced in the form of artificial gradients. In general, the bilinear interpolation technique has been used.

$$\begin{bmatrix} 1 & 1 & 1 \\ 0 & 0 & 0 \\ -1 & -1 & -1 \end{bmatrix} \begin{bmatrix} 1 & 0 & -1 \\ 1 & 0 & -1 \\ 1 & 0 & -1 \end{bmatrix} \begin{bmatrix} 1 & 1 & 0 \\ 1 & 0 & -1 \\ 0 & -1 & -1 \end{bmatrix} \begin{bmatrix} 0 & 1 & 1 \\ -1 & 0 & 1 \\ -1 & -1 & 0 \end{bmatrix}$$

Figure 1. Sample templates used for gradient computation. Weights are applied to data and weighted data are then summed. Template producing greatest value dictates the magnitude and direction of the local gradient.

A series of templates like those depicted in Figure 1 are used to compute the gradient. From the application of these templates, one can determine the magnitude and direction of the gradient around each grid point.

The gradient vectors are organized into lines through a heuristic search procedure. The vectors are sorted according to magnitude. Then, starting with the strongest gradient, we construct lines bilaterally utilizing adjacent strong gradients with consistent directions. This procedure continues until all adjacent strong gradients have been exhausted. For the remaining strong gradients, this procedure is repeated for a new line and then for all subsequent lines until all strong gradient values are used.

This technique has been extensively used for the front detection, precipitation mapping, and hurricane assessment tasks discussed below.

4. Front Detection

The gradient detection scheme described in the previous section has been applied to the detection of cold fronts. Cold fronts are contained in troughs and therefore have significant wind shear and curvature in their wind fields. In addition, lines of precipitation often accompany these fronts due to lifting of the warm air by the frontal surface. As will be seen, these wind field and precipitation features can be detected very readily using gradient detection.

The gradient detection technique discussed in Section 3 was applied to data collected by the PL Doppler radar on November 16, 1989. The original velocity data

are presented in Figure 2. Application of the technique to these data resulted in the gradient magnitude field depicted in Figure 3. Here we see a well-defined line extending from north to south. The gradient direction field (not shown) contains an associated line of coherent directions. It should be noted that aliased data produce artificial gradients that can be misinterpreted. On the other hand, the magnitude of these gradients, their organization, and the magnitudes of the velocities themselves could provide a new perspective to the solution of the velocity dealiasing problems. This aspect was not pursued in this effort.

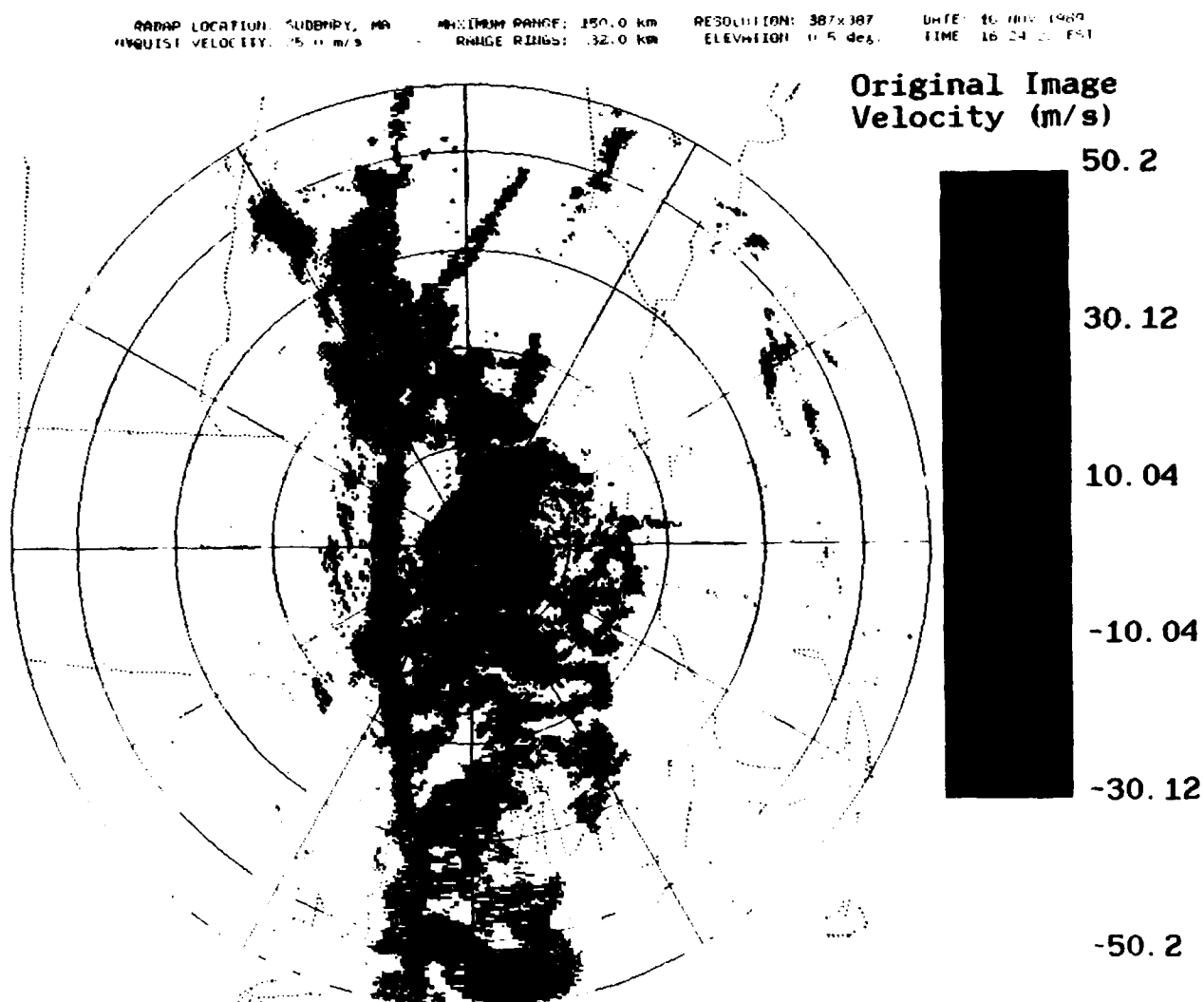


Figure 2. Doppler velocity data collected by PL Doppler radar in November 16, 1989.

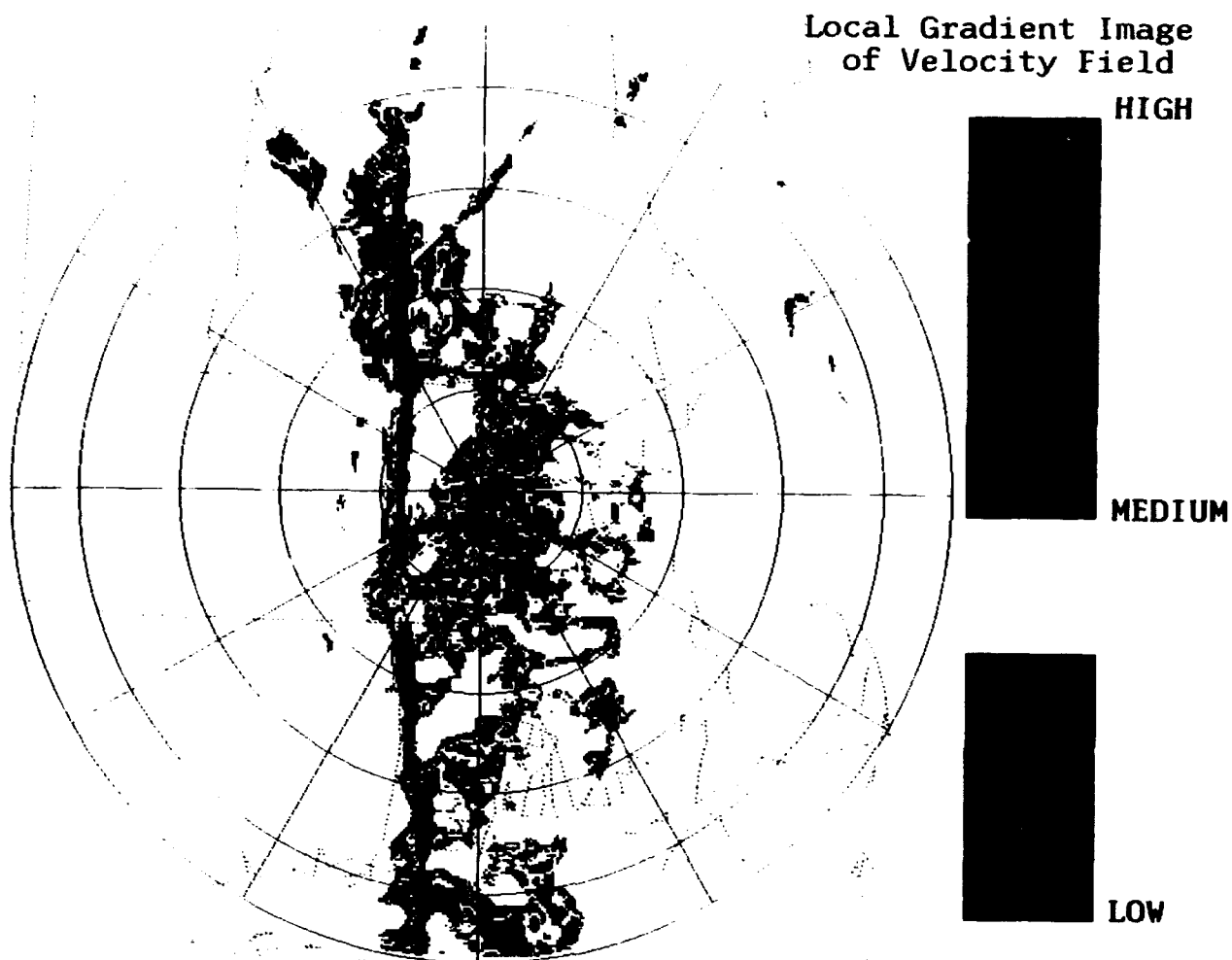


Figure 3 Gradient Magnitudes for Data Plotted in Figure 2.

From the gradient magnitudes depicted in Figure 3 and from the associated direction fields, lines of maximum gradients have been constructed. The gradient vectors are sorted according to magnitude. Values below a specified threshold are ignored in further processing. With the largest value as a starting point, a line is constructed by searching in the orthogonal direction to the gradient vector to find the largest adjacent magnitude. The line is then extended to that point and to all

successive points that satisfy the search criteria. Once one end is obtained, the starting point is revisited and the procedure is then conducted in the opposite direction until line construction is completed. All values used to construct that line are removed from the sorted list. Other lines are constructed from any remaining gradient values by starting with the largest available gradient value. The result is an array of line segments. These segments are consolidated as much as possible by extension techniques much like those used for line construction. Length thresholds are imposed and shorter segments are eliminated. For the front situation, the end result is generally two to three segments aligned along the perceived front position (Figure 4).

For the reflectivity fields, a line pair is produced, one on either side of the thin line of reflectivity along the front. The direction field contains diametrically opposed angles along each of the lines. As a result, the line construction routine assembled two lines that bracketed the band of strong reflectivity. (Figure 5). In order to develop a procedure in which both reflectivity and velocity information could be integrated, an adjustment was made to the line construction procedure so that its result would also work to generate single boundary lines. Instead of assembling lines by mapping along the gradient intensity lines, it instead travels along the lines of high reflectivity intensities. Lines from the reflectivity and velocity analyses can subsequently be merged to form a more complete representation of the front.

The gradient detection process is a promising method to isolate atmospheric fronts. This routine offers the ability to combine both reflectivity and velocity boundary information to either help strengthen or weaken a potential boundary. Future work will involve the combination of multiple elevation images to provide insight into the vertical structure of the front.

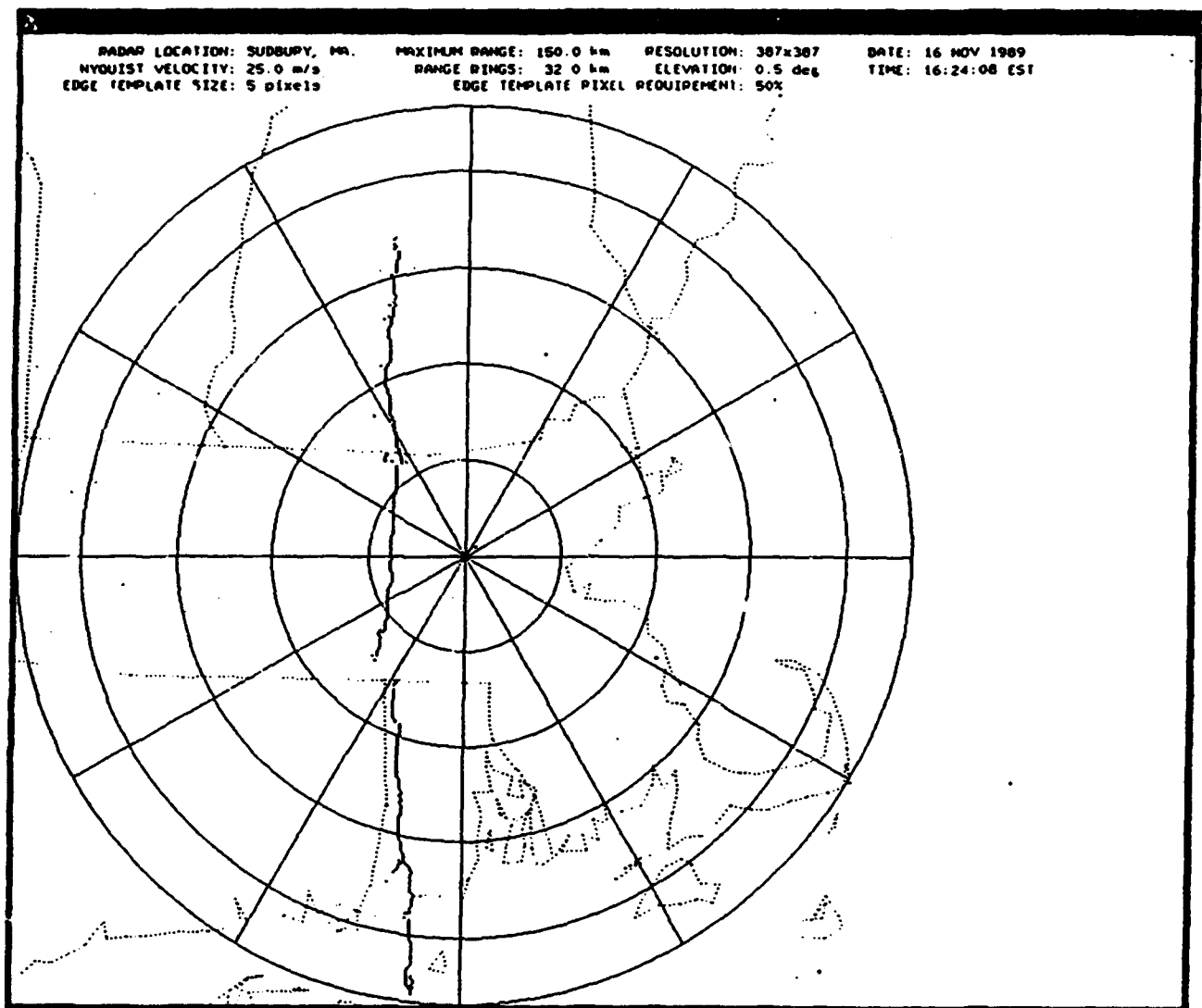


Figure 4. Lines of Maximum Gradient as Derived from Data in Figure 3.

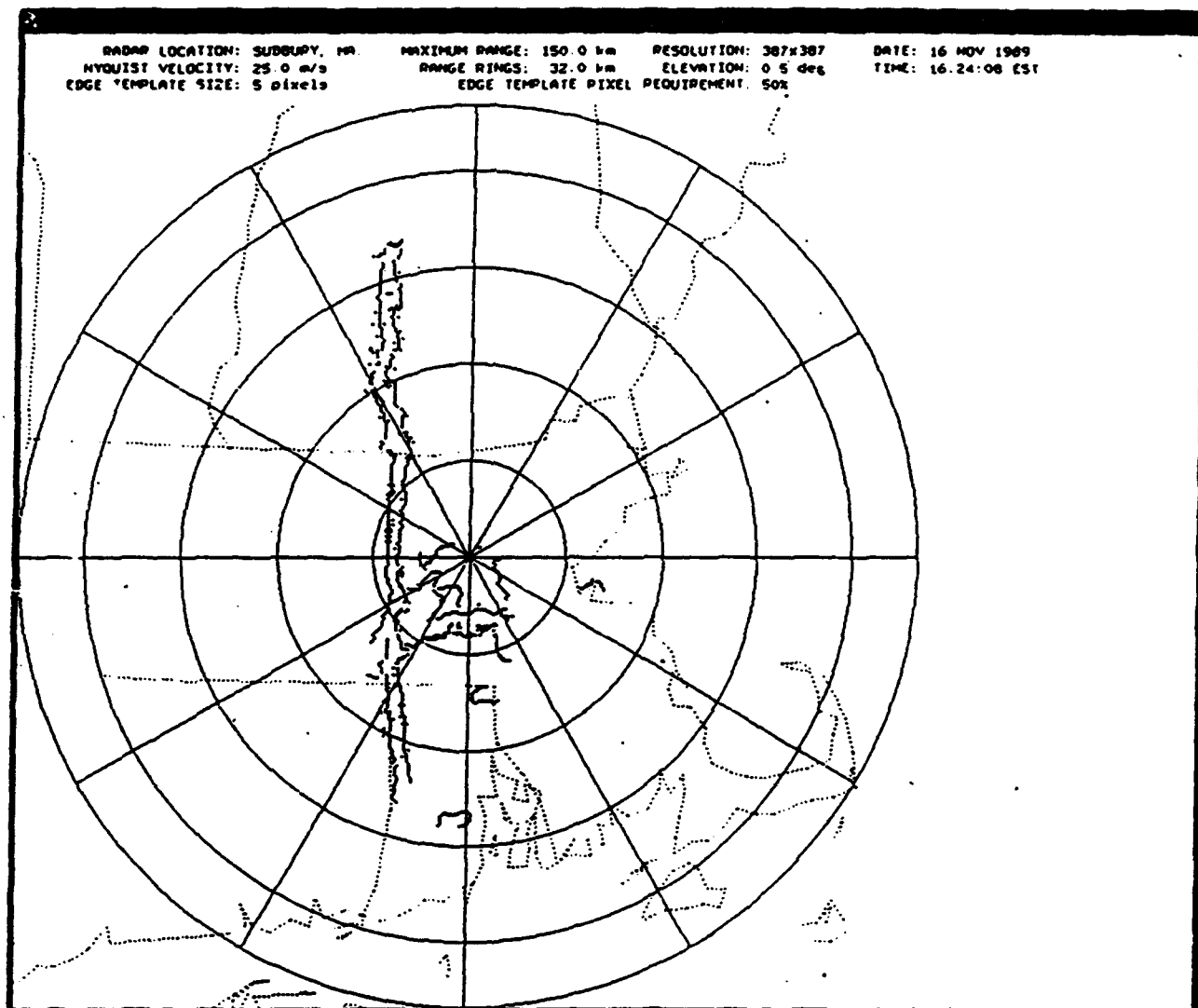


Figure 5. Lines extracted from reflectivity gradient data

5. Precipitation Location/Motion Determination

5.1. Introduction

General aviation operations and military satellite communications are often disrupted by precipitation events. Accurate forecasts of the onset and conclusion of a precipitation event benefit both the public and the military. Automated Nowcasts of these events lie within the realm of the WSR-88D Doppler Radar system. A Nowcast consists of three elements:

- detection
- tracking
- forecasting.

Automatic detection of precipitation onset and conclusion frees radar meteorologists from manually tracing precipitation areas onto the screen. Instead, they can concentrate on the dynamics of an event. Automatic tracking of an event provides immediate information on changes in direction, speed, and orientation. A Nowcast of future locations of precipitation follows from the detection and tracking results, as the information gained is extrapolated into the future. A precipitation detection and tracking process has been developed in which reflectivity contours are used to describe the outline of a precipitation event, gradient lines characterize the onset of frontal situations, and the leading or trailing edges of any precipitation areas can be identified as either a line or a contour in the detection process. Details of this technique are presented in Bals (1991).

5.2. Detection Techniques

To forecast the onset and termination of precipitation one needs to delineate the perimeter of the precipitation area. The detection techniques to be presented are based on the extraction of this perimeter. By extracting only the perimeter rather than trying to monitor the entire weather system, the amount of data needed to monitor, track, and forecast the onset of precipitation is greatly reduced. The following methods of perimeter detection and extraction were investigated:

- Precise interpolation of a constant reflectivity factor threshold defining a line (contour) of selected reflectivity.
- Extraction of an approximate reflectivity factor contour.
- Detection of the edge of a precipitation region.

The first method requires the detailed representation of a constant reflectivity contour as a collection of Cartesian coordinates. This product is time-consuming to produce and the results are difficult to use in subsequent analyses. The second method involves simply walking around the data grid while keeping data values higher than a threshold value on one side of the path. This technique will work well where the gradients are distinct and the data density is high. In stratiform precipitation events where widespread precipitation gradually moves into range, the reflectivity contours provide a good indication of the precipitation onset. In more active events, a constant Z value representation of distinct convective cells may be an incoherent pattern of scattered contours, even though the overall convection may be organized into a linear

pattern. An edge detection technique provides an alternate method in such events, as the incoherent contour pattern emerges as distinct lines of strong gradient. The combined use of a simple contour extraction technique and the edge detection technique provides the information needed to detect and track the onset and cessation of precipitation events.

5.2.1. Contour Extraction.

Once the data are interpolated onto a Cartesian grid, the contours of user-defined constant Z value must be detected and extracted from the radar data. A systematic grid point by grid point, line by line search for data values equal to or greater than the constant Z value starts from the lower, left-hand (southwest) corner of the radar display and searches to the right (east). Once the first value is found the contour extraction technique begins.

1	0	7
2	X	6
3	4	5

Figure 6. Template for specification of Freeman Chain Code.

The extraction technique "walks" around the area of values greater than the constant Z value and identifies each point of the contour. A representation of the points defining a contour with eight-point directional angles was developed by Freeman (1961) and will be referred to as the Freeman Chain Code (FCC). The FCC assigns a directional value to each point based on its location with respect to the previous point as shown in Figure 6. For example, if a point is to the right of the first point (the middle

point) it will be given the value 6, or if it lies up and to the left of the first point it will be given the value 1. This process of finding the contour point and assigning it a FCC value continues, in a clockwise manner around the area of values greater than or equal to the constant Z value, until the start point is again encountered. The contour is now defined by its start point coordinates and a series of points which create a "chain" of directional codes. Previous studies (Bohne and Harris, 1985 and Bohne et al., 1988) concluded that the Freeman Chain Code is an efficient and effective means of representing reflectivity contours. In this study we have extended the use of the chain code to describe edges.

5.2.2. Edge Extraction

The edge detection technique developed by Hamann (1991) extracts a line or a series of lines of gradient maxima from the radar data. In a frontal system the derived line image is dramatic and clearly denotes the front, since strong reflectivity and velocity gradients accompany the frontal passage. Less intense systems also benefit from this technique, since the leading edges of precipitation are usually accompanied by significant reflectivity gradients. Areas of enhanced convection embedded within an otherwise uniform precipitation echo are also delineated by the gradient lines.

5.2.3. Feature Detection

The contour extraction and edge detection techniques provide complimentary methods of delineating the start and finish of precipitation. The contour extraction technique offers a good indication of precipitation onset in widespread precipitation events, such as warm fronts, while the edge detection technique reveals the gradient

accompanying a cold front or an intensely convective storm. The edge detection technique extracts strong gradient lines, where precipitation may develop in time. Some convective storms have intense leading lines of strong reflectivity or velocity, but are trailed by widespread areas of stratiform precipitation.

The representation of the contours and lines by the FCC provides information on the features unique to each event. The area, center of area, perimeter length, and directional variation of the line can all be derived from the FCC description of the contour (Bals, 1991). Monitoring these features as they move and evolve through time will aid in the tracking of the precipitation onset.

5.3. Tracking Technique

Several studies have shown that cross-correlation and linear extrapolation are effective means of tracking precipitation area centroids (Endlich and Wolf, 1981, Zittel, 1976 and Barclay and Wilk, 1970). However, tracking echo centroids alone causes discrepancies when an echo expands or gradually moves into the radar viewing area. The center of an expanding storm may remain stationary, while the area experiencing precipitation grows. As a storm moves into the range of the radar, the true extent of the echo may not be shown on the radar display. In such a case, the center of the storm will seem to retrograde as the storm moves onto the display. By identifying a reflectivity contour which envelopes most of a precipitation area, delineating a leading (or trailing) edge of precipitation, or defining a frontal boundary through velocity and reflectivity gradients, the onset or termination of precipitation can be monitored and tracked. A least-square method of correlation, similar to one used by Bohne et al. (1988), is used to track the detected contours and edges.

In the least-square method of correlation, the FCC values of each contour are compared to the FCC values for the next observation. A contour for the first observation is broken into segments of equal length, usually 10 to 25 percent of the total chain code length. Each segment of that contour is compared to all possible segments of a contour in the next observation by computing least-squared mean differences and mean square differences between the directional values of the segments. The least-squared differences for a segment are computed on a one-to-one basis over the segment chain code length (n),

$$\text{mean difference} = \sum_i (\text{FCC1}_i - \text{FCC0}_i) / n \quad (3)$$

$$\text{mean square difference} = \sum_i (\text{FCC1}_i - \text{FCC0}_i)^2 / n$$

where the first FCC value (FCC1) of a segment is subtracted from the first FCC value (FCC0) of the earlier segment, the second from the second, and the last from the last. These individual differences are summed, and a mean difference and a mean square difference are computed for every possible segment combination. A perfect correlation would have both differences equal to zero, so that a segment pair with both the mean and mean square differences nearest to zero is assumed to represent the best possible segment correlation.

Figure 7 depicts reflectivity contours for two successive scans on May 2, 1978. Three distinct echoes are identified. The contours for each time have been divided into segments as labeled and correlations were run amongst the segments. The labeling of the segments reflects the results of the correlation process.

During severe weather, interesting contour structure, such as notches, hooks or kinks, are likely to be noted by an observer, and followed with interest as the precipitation event develops. Some features are indicative of significant weather. For example, a hook on the southern end of a convective cell contour indicates the

possibility of a tornado. Unique contour structure gives the observer, and the computer, a reference point to follow through time.

The directional variance of a segment provides an indication to the computer of which segment has more variation (more interest, in visual terms) than the other segments. Significant features on a contour will have more directional variance than the overall contour variance. The directional variance for a segment [var(seg)] of length n is the mean square difference of the individual FCC value (FCC_i) from the segment mean directional value (FCC_m):

$$\text{var(seg)} = \sum_i (FCC_m - FCC_i)^2/n \quad (4)$$

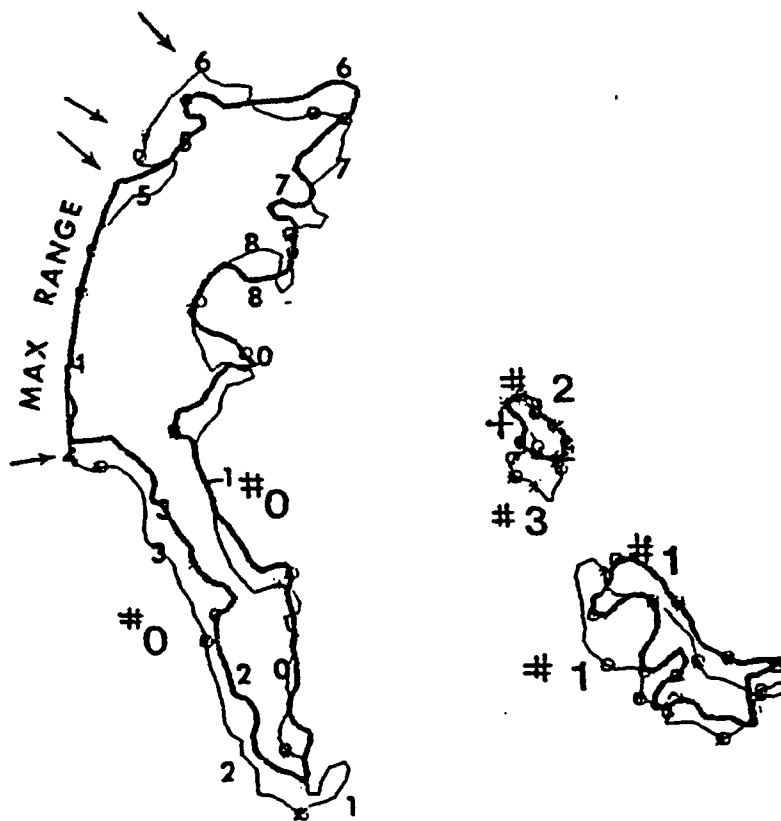


Figure 7. Reflectivity contours for two successive scans. See text for details.

Obviously, the segment length influences the variance, smaller segments do not include all the chain code of a feature, larger segments smooth out the effects of smaller features. However, the variance is only used to give the computer a starting point based on each segment's variance relative to the other segments in the contour. The first matched segment pair is the reference starting point from which the segment correlation of the contours originates.

The computed variances are compared to find the segment with the largest directional variance for each contour. The first segment pair is chosen by:

- computing the directional variance for each segment,
- finding the segment with the highest variance for each contour,
- checking to insure no portion of the segment lies along the maximum radar range boundary,
- determining the best segment match from the least-squared difference values.

The results of the segment correlations are then compared to find the best contour matches by using the following methodology:

- sort the pairings as to mean and least-squared differences
- find the largest segment size,
- determine percentage of segments in contour that have acceptable matches.

From the sorted differences, the contour pair with the largest segment size is found. A confidence factor for the contour match is established based on the percentage of segments that are matched.

Once all the contours are matched, the overall movement of the contours can be computed. Adjustments made during the segment correlation give information on expansion or decay of contours. The tracking information for each contour pair can then be used to create forecasts.

5.4. Forecasting Techniques

In a study of several forecasting techniques, two techniques (Table 1) were found by Bohne et al. (1988) to perform best for feature prediction. A simple exponential smoothing filter uses a time series of feature changes with successive observations to obtain forecasts. The Brown One-Parameter Adaptive Smoothing filter bases its forecast on the original feature observations. Both techniques develop future segment features from observed features.

Table 1: Basic Forecast Formulations

(1) Simple Exponential Smoothing Filter

$$F(t+1) = W \cdot X(t) + (1-W) \cdot F(t)$$

(2) Brown One-Parameter Adaptive Smoothing Filter

$$F(t+1) = A(t) + B(t) \cdot m$$

where

$$A(t) = S_1(t) + (S_1(t) - S_2(t))$$

$$B(t) = (S_1(t) - S_2(t)) \cdot (W/(1-W)) \text{ and}$$

$$S_1(t) = W \cdot X(t) + (1-W) \cdot S_1(t-1) \quad S_2(t) = W \cdot S_1(t) + (1-W) \cdot S_2(t-1)$$

$X(t)$: current observation

$F(t+m)$: forecast for next observation

W : user defined weight

t : current observation time

m : intervals from current time

5.5. Conclusions

Two precipitation perimeter extraction techniques and a precipitation tracking technique have been developed and tested. A contour extraction technique, combined with an edge detection technique, defined and delineated major precipitation areas for a variety of synoptic and mesoscale situations. The Freeman Chain Code representation method described the results of either detection technique in an efficient and space-saving manner.

The tracking technique scans the Freeman Chain Code values of the contours to find unique features and uses characteristics of those features to initiate the contour matching procedures. Contours were matched section by section based on a least-squared difference analysis of their Freeman Chain Code values. Contours which had the best sectional matches were considered, after further scrutiny, as contour matches.

The technique was applied to three different precipitation events (Bals, 1991). Overall, the leading edges of precipitation areas were successfully matched to the corresponding leading edges of the next observations. Similarly, trailing edges from successive time periods were matched.

Improvements in the detection technique will lead to improvements in the tracking technique. Creating composite reflectivity fields and controlling the reflectivity factor threshold level will contribute to more consistent contours. As part of future research, the following factors in the tracking technique need to be investigated:

- Least-squared difference thresholds for inappropriate matches.
- Check for unrealistic motions between observations.

- The role of contour directional variance as precipitation evolves with time.

Implementation of the forecasting techniques using the results of this tracking technique provide a useful tool for operational forecasting of precipitation onset and conclusion.

Detailed analyses are presented in Bals (1991).

6. Precipitation Type Estimation

6.1. Introduction

Precipitation at or near the ground can cause significant problems, the severity of which depends upon the precipitation type (e.g. snow, rain, or freezing rain).

Accumulation of snow and the coating of structures and the ground due to freezing rain will at very least impair operations and, at worst, cause serious accidents and loss of life. A study was conducted to develop techniques that will determine precipitation type. Details of the study itself are contained in Harris and Smalley (1993). In this report only a summarization of the resultant algorithm will be presented.

6.2. Algorithm Definition

6.2.1. Precipitation Phase Detection

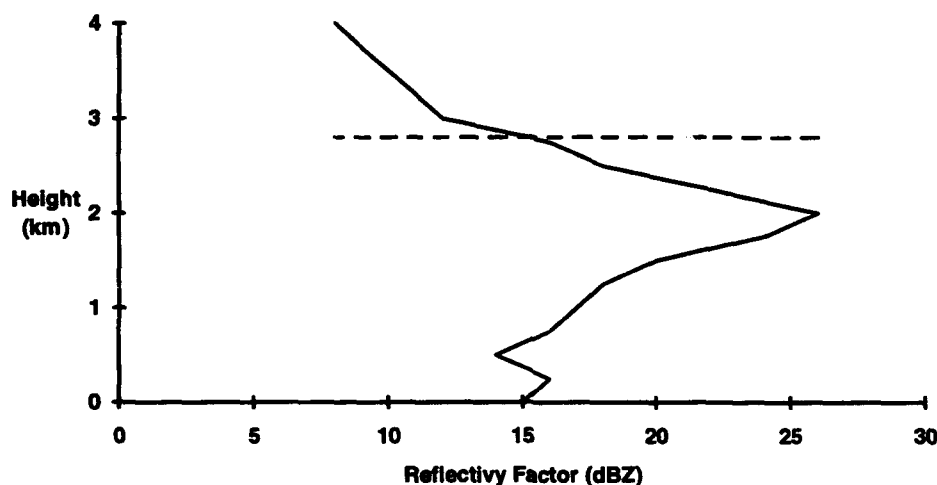


Figure 8. Schematic of reflectivity factor vs. height. Dashed horizontal line indicates height of 0° C isotherm.

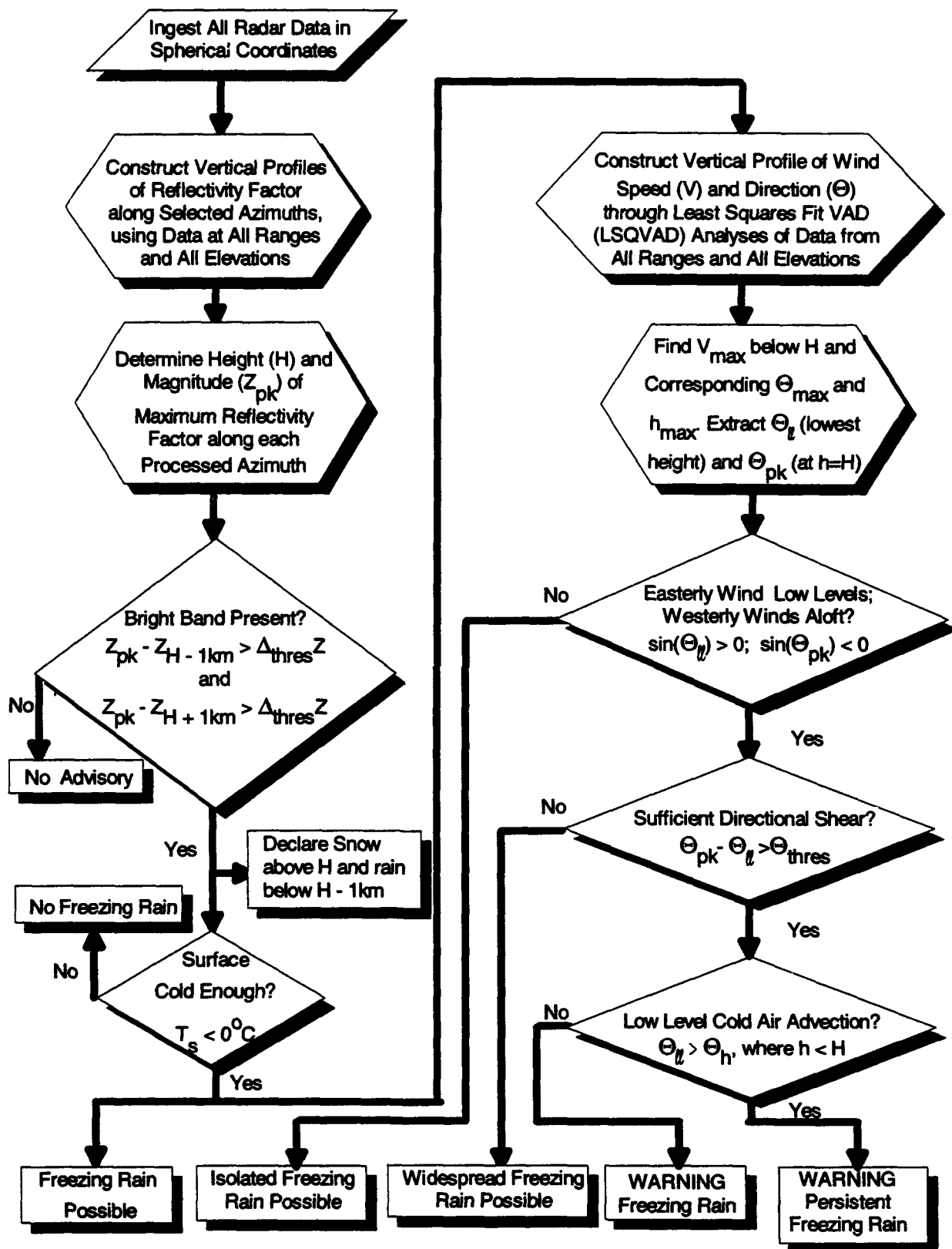


Figure 9. Flow Diagram for Precipitation Type/Freezing Rain Algorithm

The first step in freezing rain detection is precipitation phase detection. The technique that we used to detect precipitation phase is simply a bright band detection scheme, one designed to detect reflectivity factor profiles like that in Figure 8. Figure 9 depicts a flow chart for the processing of radar data for the entire Freezing Rain Algorithm. The section on the left pertains to bright band detection and has as an end product an indication of the location in the vertical of rain and snow.

The data are processed for specified azimuth angles. These beams would be operator selected to allow reasonable assessment of the precipitation structure in the vicinity of the radar. Data from all ranges and for one (the highest) or all elevation angles are extracted and heights assigned. The data are then sorted with respect to height and presented as a vertical profile for each of the selected azimuths. Maxima (Z_{pk}) are extracted from each profile along with their corresponding heights. Reflectivity differences are then computed both above and below the maximum to ensure that the maximum is sufficient to correspond to a melting layer. A threshold (Δ_{thresZ}) is specified, with a recommended value being 6.7 dB. If both gradients pass the threshold test, a bright band is declared. One can then say that there is snow above level H and rain below H - 1 km.

6.2.2. Freezing Rain Detection

Determination of the existence or potential for freezing rain events relies very heavily upon the above described bright band detection algorithm. In fact, with just the bright band detection scheme and surface temperature observations of less than 0°C, it is reasonably safe to say that there will be freezing rain somewhere in the vicinity of the radar. However, it is possible to better specify the nature and duration of the freezing rain event through a consideration of the wind field. Freezing rain events will tend to develop and/or persist if there is a low level easterly wind with a southwesterly

overrunning air mass. In addition, it is anticipated that in marginal situations, cold air advection in the lowest levels will tend to enhance the potential for freezing rain. It will also tend to prolong the event.

The algorithm requires the computation of VAD estimates of wind speed and direction, preferably at 1 km range resolution and at all elevation angles. The least-squares-fit of at least a third harmonic Fourier series is required. Simple harmonic analyses can produce significant errors. Vertical profiles are then constructed for the wind speed and directions and 5th order power law curves are fit to each. The maximum wind speed (V_{\max}) below the bright band peak is estimated from the fitted curve. The height for that peak (H) is recorded and the corresponding direction (Θ_{\max}) for that height on the power law curve for the directions is determined. The directions for the lowest height ($\ell\ell$) and for the peak in the reflectivity pattern are extracted from the fitted curve at the height of the lowest data point and the height of the peak reflectivity.

One necessary and sufficient condition for freezing rain declaration is the detection of the bright band and surface temperatures less than 0°C . However, to provide qualitative assessments of the seriousness of the freezing rain event, other conditions based upon the wind field structure are imposed. The first wind condition to be imposed is that there is an easterly flow in the lowest levels and a westerly flow aloft. *This is really a condition on the preferential directions for flow ahead and behind a warm front, the most likely situation for substantial freezing rain.* This test can be refined and/or adjusted to local climatology to account for different preferred wind conditions. For example, for New England, the condition could be adjusted for $0 < \Theta_{\ell\ell} < \pi/4$ and $\pi < \Theta_{pk} < 3\pi/2$. The rationale for the sufficient directional shear criteria is that for freezing rain conditions to be persistent there should be at least some component of

the low level wind opposing the influx of warm air aloft. In fact, it is logical to assume that the greater the opposition of the low level flow, the greater is the probability that the freezing rain will be persistent. In addition, if the profile indicates cold air advection near the ground (i.e, the winds back with height just above the ground) there is an even greater probability that the freezing rain will be persistent and widespread.

6.3. Future Considerations

There are many other influences on the detection/forecasting of precipitation type. These include

- intensity of precipitation
- warm air advection
- temperature profile assessments
- humidity profile

6.4. Conclusion

Under this task we have developed an algorithm for the detection of precipitation type with particular emphasis on freezing rain. The algorithm shows considerable promise but requires much more testing/evaluation.

7. Hurricane Location Determination

7.1. Introduction

Accurate tracking and forecasting of hurricanes is vital for safe aircraft operations. Damage from the winds and from the torrential downpours of a hurricane, especially those near the eyewall, can be devastating. Monitoring the location and movement of the eye can give the needed warning to minimize damage, or conversely, to prevent unnecessary time and money spent in preparation for a hurricane landfall which does not occur. Over the years much attention has been paid to locating and tracking the eyes of hurricanes. Satellites are invaluable in locating hurricanes and typhoons, but cloud cover can obscure the hurricane eye location. Assuming that the hurricane eye is at the center of a huge cloud mass can be dangerously incorrect because the tropical storms may encompass large areas and often have asymmetrical orientations. Research planes monitor hurricanes which approach the East Coast of the United States, but such careful scrutiny is expensive and not amenable to real-time data dissemination. Also there are insufficient aircraft to cover all tropical storms in all locations at all times.

Doppler radar sees through the clouds that obscure a satellite's view. A ring or rings of strong reflectivity are usually seen around the eye of a mature hurricane. Further out from the center, the reflectivity structure characteristically contains precipitation bands which spiral outward from the hurricane eye. These bands begin to appear on the radar display hours before the full force of the hurricane reaches the radar. Identification of the visual image of the spiral bands and representation of their structure as physical boundaries are done through an image analysis technique. In this report we will present a technique to estimate the location of hurricane eyes based on

radar detection of the precipitation structure. The location of the precipitation boundaries re examined to determine their utility in locating the eye.

7.2. Technique

The hurricane eye detection technique is based on the assumption that the precipitation bands are oriented around the hurricane eye and that lines orthogonal to the bands will pass through the hurricane eye. Intersection of pairs of orthogonals at different points on the same band are then assumed to provide estimates of the eye location. Quite obviously this approach should work best for those bands closest to the storm center. We intend to assess its utility when only the outer bands are visible.

Because hurricane rain bands tend to have distinctive gradients along their edges, the Hamann gradient detection technique was implemented. With this technique the reflectivity gradients (both magnitude and direction) along the outside boundaries of the bands can be determined.

Lines orthogonal to the bands are constructed through use of one of two methods. The first method assumes the reflectivity gradients along the precipitation bands are locally normal to the bands and have directional values toward the hurricane eye. Lines are constructed from each point on the bands where the slope is determined by the gradient directional value. While this technique is easy to implement, the angular slopes are restricted to multiples of 45° . The second method breaks the band into small segments and constructs a perpendicular for each segment. This method does not have the angular resolution restriction, but is more time consuming to implement. Once lines are constructed by either method, intersection points are computed from pairs of lines from either the same band or from two different bands.

7.3. Analysis

Even though data were available for two hurricanes (Hurricanes Gloria in 1985 and Bob in 1991), both storms had decayed so much that they did not exhibit the usual band and eye configurations that we have become so accustomed to seeing in healthy hurricanes. As a result, we resorted to the use of simulated data constructed for NEXRAD algorithm development by Wood and Brown (1987). Using analytically derived hurricane reflectivity and flow fields, they developed a scenario in which a hurricane approaches a coastline where a 10-cm Doppler radar is located. The model is evaluated on a three-dimensional array, whose domain is 300 km in the horizontal directions and 14 km in height. The grid intervals on the horizontal plane are 2 km, and 1 km in the vertical. These data are then used for the application of the eye detection schemes.

The first step in the analysis process is rain band detection. However, even for the simulated data, the resultant bands tended to be somewhat fragmented. Therefore, techniques were developed to join these segments into more coherent bands. The process of band extension/merging is identical to that used for band construction except that the shear threshold has been lowered.

Figure 10 depicts the reflectivity factor field for the hurricane data at 2224 GMT. This time was chosen for testing the techniques since the center of the hurricane can be estimated fairly accurately within the radar display grid. The "true" eye location was estimated to be in the exact center of the innermost reflectivity ring, at 65 km radius along the 110° azimuth angle from north. The Cartesian location of the hurricane eye is at 61.08 km east and 22.23 km south of the radar origin. These are the "truth" values against which technique estimates are compared.

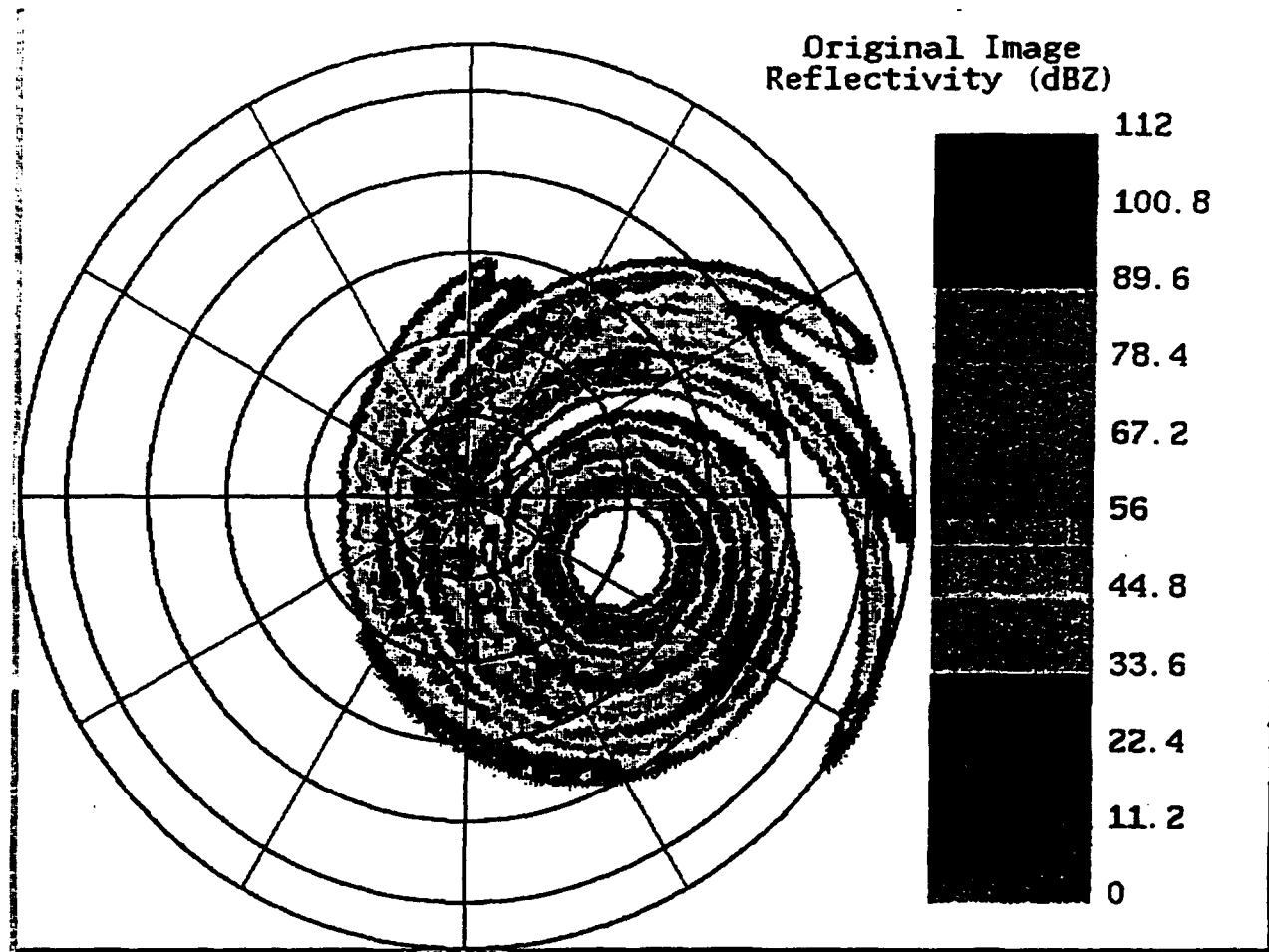


Figure 10. Simulated radar reflectivity factor data used for evaluation of hurricane eye algorithm.

Figure 11 is a plot of lines of gradient maxima and estimated hurricane center points for four methods using all lines. The first two techniques use the gradient directions to compute the lines. The first one (directional-single) computes intersections for lines from the same band while the second (directional-double) utilizes

lines from different bands. The next two techniques use normals to line segments and compute intersections of normals from the same (slope-single) and from differing (slope-double) bands. All four methods give fairly reasonable results.

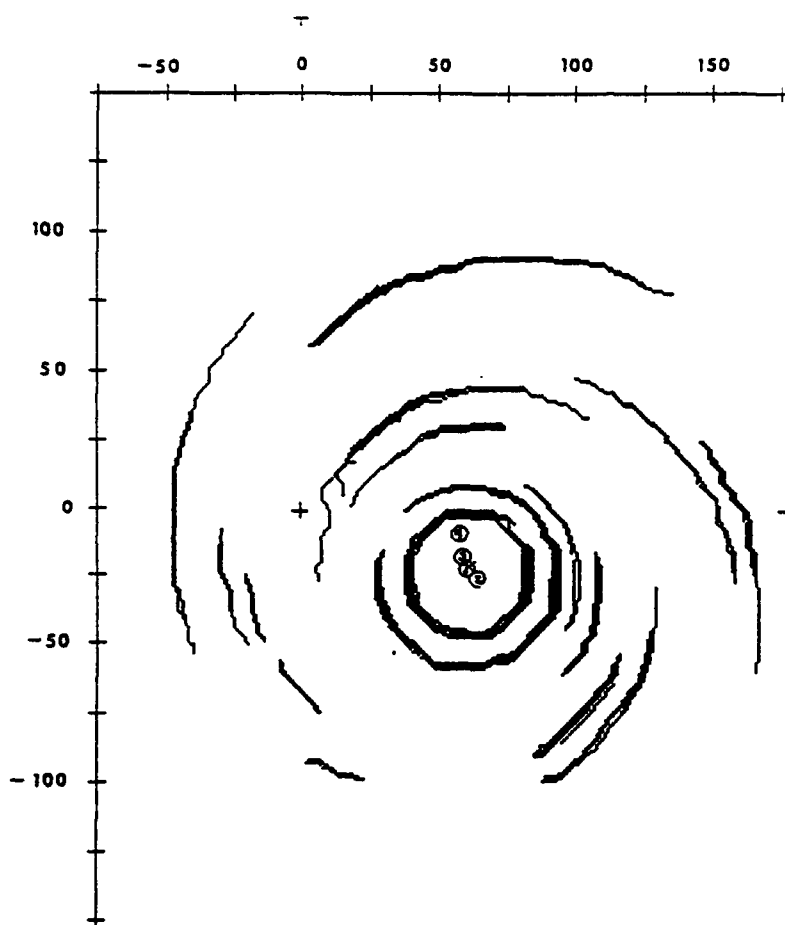


Figure 11. Center estimates for four estimation techniques.

By applying distance thresholds, we were able to simulate less than perfect coverage of the storm. Figure 12 shows the differences in the individual x and y coordinates from the "true" eye location for each method as a function of threshold distance. The directional-single method produces estimates of x within 1 km of truth

out to 40 km and y estimates within similar errors out to 70 km. Beyond those ranges, there is a marked increase in the y-component error to 35 km and x-component errors of 5 to 12 km. For the slope-single method, the x-component estimates are within 5 km of truth at all ranges, while y values have similar errors out to 70 km, but increase significantly beyond.

Both components of the directional-double method vacillate around the "true" coordinates and are too erratic to be trusted. In contrast, the slope-double results are consistent at all threshold distances. The x-component of the slope-double technique remains within 5 km of the "true" center at all threshold ranges. The y-component is consistently located from 12 to 9 km north of the "true" center. At the larger thresholds this value is an improvement over the directional-single and slope-single estimates. From these figures, it appears that the directional-single method produces the best results when the hurricane is within the field of view. When only the outer bands are observed, the slope-double technique produces the best results. However this technique as applied here will produce a significant northern bias. When we examined the scatter of points about the mean for each of these estimates, it was found that the least scatter occurred for the two techniques that utilized lines from different bands. However, these techniques produced the greatest biases.

The effects of excluding points far from the estimated mean were examined. The best results for the directional-single method occurred when all points were included. However, both the slope-single and slope-double estimates improved when only values within one standard deviation were included.

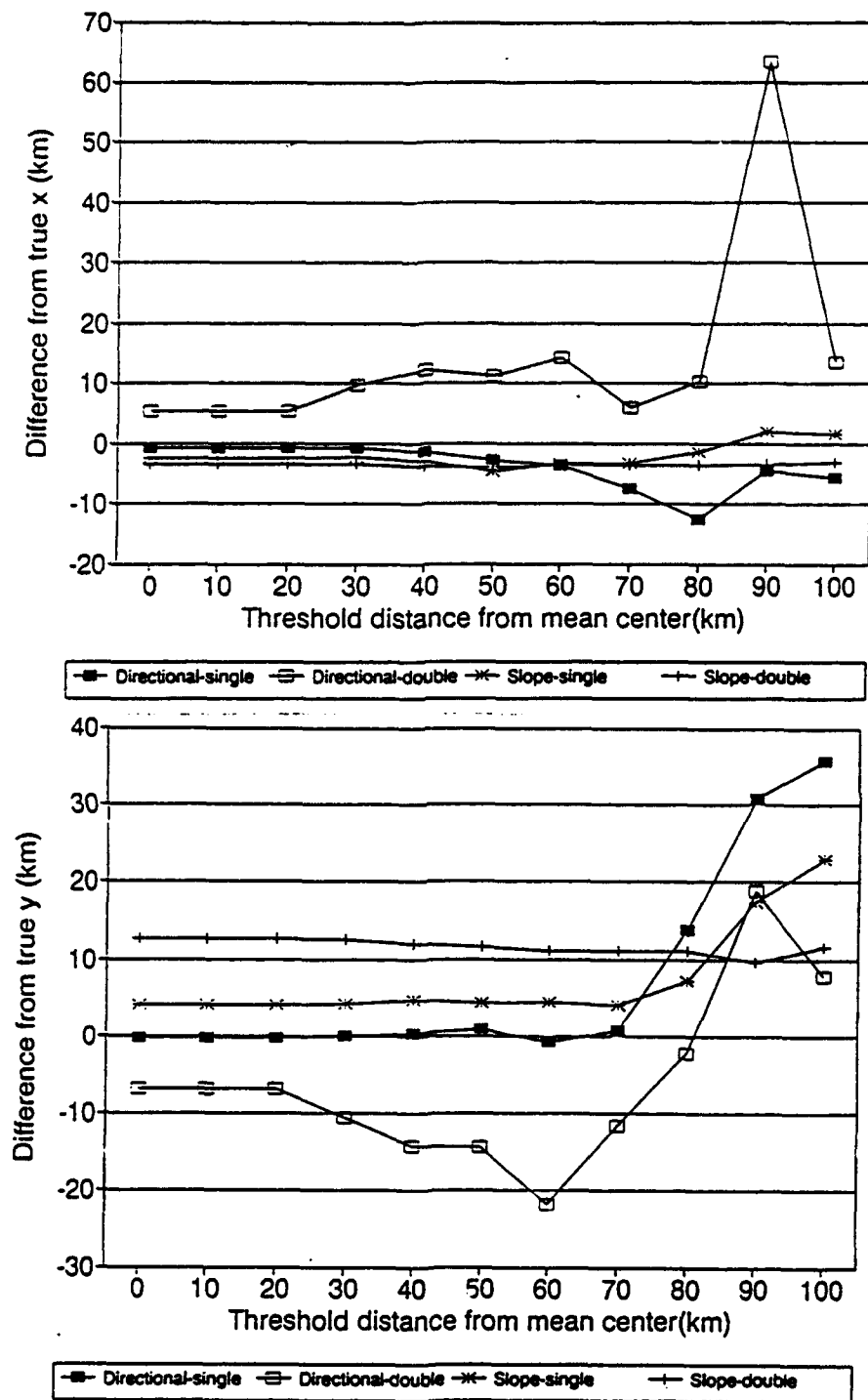


Figure 12. Differences in the x (a) and y (b) coordinates from the "true" locations as a function of threshold distance.

7.4. Summary

Four techniques to locate the center of a hurricane from the reflectivity structure of the hurricane were explored. All of the techniques were based on a simple premise: locate the hurricane eye by intersecting lines perpendicular to the curvature of the precipitation bands. Two methods of constructing these lines were utilized in the four techniques. Two of the four techniques, directional-single and slope-single, were found to be fairly accurate at estimating the hurricane center for precipitation bands within 70 km of the hurricane eye. A third technique, slope-double, while not as accurate as the first two techniques, produced a consistent result, even for hurricane outer bands appearing on the periphery of the radar range. A fourth technique, directional-double, was too inconsistent in locating the hurricane center to be recommended as a useful technique.

The directional-single technique involves the fewest computations. The slope of the intersecting lines is taken directly from the description of the hurricane bands given by the edge detection algorithm. The mean center points are within 10 km of the hurricane center for bands within 70 km of the center, and the center points are nearly perfect for bands within 40 km. However, the relatively coarse resolution of the slope angles, results in a large amount of scatter and contributes to the accuracy deterioration as the distance threshold increases.

Better resolution of the slope angles produces less scatter in the individual center points of the slope-single technique. Though not as accurate at the closer thresholds as the directional-single points, the mean center points are still within 10 km of the hurricane center. At the larger thresholds the accuracy of the slope-single mean center coordinates diminishes, but not nearly as much as the directional-single results.

Calculating from a limited number of streaks in the outer northwest bands of the hurricane produced a center point only 16 km away from the "true" center.

The slope-double technique requires the most calculations and produces the most consistent results at all the distance thresholds, within 9 to 12 km of the "true" center. The mean center points at the largest distance threshold are more accurate than the other two techniques, but at the smaller thresholds the accuracy of the center coordinates is not as good as the two other techniques. Limiting the results of the individual center points within one standard deviation of the mean center point improved the accuracy of this technique to within 6.5 to 9 km of the "true" center.

Overall, these techniques show promise as a practical means of automatically calculating the eye of a hurricane. The directional-single and slope-single techniques give the best results at close range. At longer ranges, as the hurricane approaches the radar and less data is available, the slope-double technique seems to give the most consistent estimate. The limited streaks shown in the last figures resulted in fairly reasonable center estimates. This is encouraging for monitoring the approach of hurricanes while their centers are still out of range of the radar. Though not perfect, these techniques placed the estimated eye well within the eyewall of this synthetic hurricane.

Future research with real hurricane data and more investigation into the biases noted in the techniques could result in a fairly accurate and fairly simple routine to quickly and automatically locate the eye of the hurricane. Limiting the separation distance along streaks when computing orthogonals might reduce the influence of the increasing radius of curvature in the spiral rain bands. When the eye is within range, the first estimate of the center could be used to isolate the inner bands and further

refine the center estimate. Once the inner bands are detected their dimensions can be monitored and tracked over time. All of these factors should combine to increase the accuracy and potential usefulness of this technique.

8. Hurricane Intensity Estimation

8.1. Potential Vortex Fit

Considerable effort under a previous contract and during the early stages of this one was placed in the development and evaluation of a hurricane intensity evaluator called Potential Vortex Fit (PVF). It basically involves the evaluation of how well the hurricane circulation matches a potential vortex flow field. This effort has been published in the refereed journals and in numerous conferences. As a result, this effort will not be reiterated here. However, one thing that is lacking in all of that literature is a description of a PVF estimation algorithm. In this section we will address this need.

The method uses VAD (Velocity Azimuth Display) data consisting of Doppler velocities acquired at constant range (r) and as a function of azimuth. The radar antenna should be scanning at a low elevation angle ($> 10^\circ$). In addition, one needs to know the range (R) and azimuth (α_s) of the cyclone center from the radar plus its translational speed (v_s) and direction (α_s). These parameters can be determined from the radar data if the storm eye is within viewing range (as derived in the previous section), from satellite image derived estimations, or from official National Weather Service estimates based on a variety of sources. It should be noted that any estimates derived from other than radar data will be old and will require projecting to the time of radar observations.

A standard VAD analysis is required at a user-defined range. The range selected must be one for which there is no gap of greater than a specified threshold (e.g. 30°) and for which there is at least a specified percentage (e.g. 75%) of the total possible data. If applied to data that do not conform to these restrictions, the estimates become somewhat noisy. Results from these calculations will be the coefficients of

Eqn. 1, namely, a_0 , a_1 , a_2 , b_1 , and b_2 . These are coefficients relative to north. It is necessary to convert the values to those (a'_1, b'_1, a'_2 , and b'_2) relative to the axis joining the radar to the cyclone eye using

$$\left. \begin{aligned} a'_1 &= a_1 \cos \alpha_e + b_1 \sin \alpha_e \\ b'_1 &= b_1 \cos \alpha_e - a_1 \sin \alpha_e \\ a'_2 &= a_2 \cos 2\alpha_e + b_2 \sin 2\alpha_e \\ b'_2 &= b_2 \cos 2\alpha_e - a_2 \sin 2\alpha_e \end{aligned} \right\} \quad (5)$$

Next, calculate the following in the cyclone frame of reference

Tangential Speed: $v_T = b'_1 - v_s \sin \alpha_s$

Radial Inflow Speed: $v_R = a'_1 - v_s \cos \alpha_s$ (6)

PVF: $PVF = b'_2 R / v_T r$

Now PVF can be calculated as a function of time. Use of this parameter is as follows:

- if $PVF < 1$ and is increasing, the hurricane intensity should be increasing.
- if PVF is decreasing, the hurricane intensity should be decreasing.

This parameter has been applied to extremely limited and biased data. As a result, it should be tested on a much larger data set before being used operationally.

8.2. Radial Confluence Index

The concept of radial confluence as an estimate of tangential curvature of a cyclonic wind field was initially discussed by Donaldson (1991). In that paper, the downwind shear of the tangential wind component was recognized as a contributor to the expression derived therein for the confluence of the radial component of wind, but no attempt was made to evaluate it. Recent efforts to evaluate tangential downwind shear are described in the subsequent discussion.

The reader might appreciate a brief background review of the appropriate parts of Donaldson (1991): Harmonic analysis of the Velocity Azimuth Display (VAD) can provide values of divergence, wind speed and direction, and the stretching and shearing deformation (but not vorticity) averaged around the circle observed at constant range about a Doppler radar. The downwind shear of the tangential component ($\Delta V_T / 2r$) is equal to half the sum of divergence (a_0 / r) and stretching deformation Error! Objects cannot be created from editing field codes. along the tangential direction, and the diffuence of the radial component (demonstrated by Donaldson and Harris (1989) to be well approximated by V_R / R_C) is half the difference of divergence minus stretching deformation along the radial direction. In these expressions, r is the radius of the VAD circle, ΔV_T is the increase in speed of the tangential component of wind from the upwind side of the VAD circle to its downwind side, V_R is the speed of the radial component of wind, considered to be positive for inflow toward the cyclone center, $1/R_C$ is the radius of curvature of the tangential component, a_0 is the zeroth harmonic, and a_2 one of the components of the second harmonic of the VAD analysis.

The components of deformation are of second order and vary with twice the sensitivity to directional changes as the components of wind velocity. The radial direction is shifted 90° from tangential, so the stretching deformation is shifted 180°

from radial to tangential reference. Accordingly, the expressions for radial diffluence and tangential downwind shear are identical. We interpret this to mean that both are contributors to the same half-sum of divergence and stretching deformation, expressed by writing:

$$(a_o - 2a_2) / 2r = V_R / R_C + \Delta V_T / 2r \quad (7)$$

Manipulation of (8-1) gives an expression for R_C :

$$R_C = 2rV_R / (a_o - 2a_2 - \Delta V_T) \quad (8)$$

If we have a reasonable well-behaved cyclone, with radial flow toward the center (V_R positive by our convention), the radial component will be confluent, rather than diffluent. Since confluence is diffluence with a negative sign, R_C will necessarily be negative. This, of course, requires the denominator of (8) to be negative, which seems to be quite reasonable, as inflowing confluence implies convergence, i.e. negative a_o . Diffluent outflow, requiring divergence, and with V_R defined as negative, would also result in negative R_C . After calculation of R_C from (8), we will formulate a radial confluence index (RCI) as a positive ratio of tangential curvature estimated by the magnitude of radial confluence $|1/R_C|$ to tangential curvature estimated by distance from radar to cyclone center ($1/R$); that is $RCI = -R/R_C$.

It is not easy, though, to find a reasonable estimate of ΔV_T . We first tried an analytic approach, focusing on the total hurricane wind V_H as depicted in Figure 13. In the hurricane's frame of reference, its total wind speed V_H is $(V_R^2 + V_T^2)^{1/2}$, oriented clockwise from V_T by an angle $\Delta\alpha = -\tan^{-1}(V_R / V_T)$. Note that with both V_R (*inflow*) and V_T (*cyclonic*) positive in our system, $\Delta\alpha$ is negative, meaning that V_H is oriented

counterclockwise from V_T . New deformation coefficients a_2' and b_2' are calculated for the direction of V_H using the standard formula for shift of polar coordinate origin:

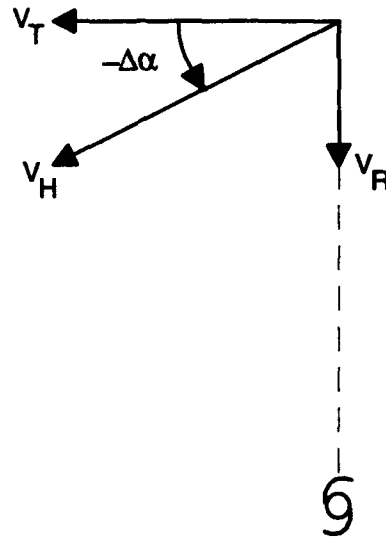


Figure 13. Tangential (V_T) and Radial (V_R) components of hurricane wind vector (V_H).

$$\left. \begin{aligned} a_2' &= a_2 \cos 2\Delta\alpha + b_2 \sin 2\Delta\alpha \\ b_2' &= b_2 \cos 2\Delta\alpha - a_2 \sin 2\Delta\alpha \end{aligned} \right\} \quad (9)$$

As the next step, we note that the downwind shear in the V_H direction is given uniquely by $(a_o - 2a_2') / 2r$, since there is no wind normal to V_H and hence no possibility for ambiguity-creating diffluence. Consequently, one of the terms of ΔV_T is $(a_o - 2a_2') \cos \Delta\alpha$, which is the tangential component of the V_H downwind speed increase across the VAD diameter. However, we must also estimate the crosswind contribution of V_H to ΔV_T .

The crosswind shear of the total wind vector is not easily available, as it is the shearing deformation in the total wind direction ($2b_2'/r$) minus an unknown curvature term. We must acknowledge some uncertainty (at this time) in how curvature varies (if at all) from its maximum in the tangential direction with directional changes away from tangential as radial components are added.

Current thinking allows room for an unknown function $f(\Delta\alpha)$ as a multiplier in the expression for curvature. In most general terms, accordingly, curvature of the total (radial plus tangential) hurricane wind is estimated as the curvature of the tangential component ($V_T / -R_C$) multiplied by $f(\Delta\alpha)$. Note that the negative sign in front of R_C converts curvature to a positive number, because if R_C can be used to estimate curvature it will necessarily be negative, following the discussion attendant to (8).

Therefore, with this approach,

$$\Delta V_T = (a_o - 2a_2') \cos \Delta\alpha + 2r(2b_2' / r) \sin \Delta\alpha - 2r(V_T / -R_C) \sin \Delta\alpha f(\Delta\alpha), \quad (10)$$

and if we note that $\sin \Delta\alpha = -V_R / V_H$ and that this substitution in the last term of ΔV_T will provide a factor $V_T / V_H = \cos \Delta\alpha$, we have

$$\Delta V_T = (a_o - 2a_2') \cos \Delta\alpha + 4b_2' \sin \Delta\alpha - (2rV_R / R_C) \cos \Delta\alpha f(\Delta\alpha). \quad (11)$$

From (8) we see that $2rV_R / R_C = a_o - 2a_2 - \Delta V_T$, and combining this with (11) and collecting selected terms, we have

$$(2rV_R / R_C)[1 - \cos \Delta\alpha f(\Delta\alpha)] = a_o - 2a_2 - (a_o - 2a_2') \cos \Delta\alpha - 4b_2' \sin \Delta\alpha. \quad (12)$$

A sample calculation in Hurricane Bob (1991) at 1203 EST, a high-quality scan, yields $RCl = 3.94$ if we assume $f(\Delta\alpha) = 1$ and 2.04 if we assume $f(\Delta\alpha) = \cos(\Delta\alpha)$.

Clearly these are inconceivably much too high since $RCI \sim 1$ would be expected in a normal cyclone. We shall briefly consider some possible error sources, including $f(\Delta\alpha)$, radial wind speed V_R , and direction to cyclone center.

Examination of a very simple model of a spiral wind field suggests that $f(\Delta\alpha) = 1$, at least up to magnitudes of $\Delta\alpha$ as high as 45° . Our model indeed had $\Delta\alpha = -45^\circ$, with $V_R = V_T$. The general spiral cyclonic wind field with zero crosswind shear and zero downwind shear can be described by the following equation:

$$V_D(\alpha) = \rho^{-1/2} [V_T \sin \alpha + V_R (\cos \alpha - r / R)], \quad (13)$$

where the new symbol $\rho = 1 + (r/R)^2 - 2(r/R) \cos \alpha$, and we are using the same coordinate system as before with α (radar azimuth angle) increasing clockwise and zero toward cyclone center. (Derivation of (13) is available upon expression of great interest.) Using (13) with $V_R = V_T = 1$ and $r/R = 0.2$, we found values of V_D and the Fourier arguments at α increments of 15° , and found the following coefficients (within a percent or two): $a_1 = b_1 = 1$ as expected from $V_R = V_T = 1$ and zero translational speed, $a_0 = -0.2$, and $a_2 = b_2 = 0.1$. From these we get $RCI = 1$, as it should be in this simple, well-behaved model. Because the model has no shear in any direction, $\Delta V_T = 0$, and solving (11) for this shearless condition yields $f(\Delta\alpha) = 1$. Eventually, this result should be checked with some shear built into the model and with other ratios of V_R / V_T .

Next, we checked for the effect of errors in estimating radial wind speed, V_R . Throughout our study of hurricanes, we have considered that the wind field measured by the radar is the sum of the wind field of the hurricane in its own frame of reference, plus a translational velocity calculated from the space - time track of the hurricane center. This may be a reasonable estimate at altitudes "above a frictional layer" and at distances "not remote from" the hurricane center. We have not discovered a radar

technique to shed some light on the two phrases in quotes in the previous sentence. Pending the development of better information, we have adopted the simple stratagem of subtracting translational velocity from the radar measurements in order to reveal the hurricane's wind field. We know that this is not correct, but we have no justification to do this differently. We must leave open the possibility that our estimates are subject to modification.

With this thought in mind, we examined the effect of reduced V_R on the calculation of RCI . At 1203 EST, one of our favored high-quality scans in Hurricane Bob (1991), the calculated V_R was 12.85 m/s owing almost entirely to the speed of translation toward the radar, because in the radar's frame of reference the velocity component toward the hurricane center was only 0.16 m/s. So we tried new calculations of RCI at fractional values of the original V_R , at each step recalculating $\Delta\alpha = -\tan^{-1}(V_R / V_T)$ and assuming no change in V_T . We found it helpful to combine equations (9) and (12), with $f(\Delta\alpha) = 1$, to arrive at

$$2rV_R / R_C = a_0 - \frac{2a_2(1 - \cos\Delta\alpha \cos 2\Delta\alpha - 2 \sin\Delta\alpha \sin 2\Delta\alpha) - 2b_2(\cos\Delta\alpha \sin 2\Delta\alpha - 2 \sin\Delta\alpha \cos 2\Delta\alpha)}{1 - \cos\Delta\alpha} \quad (14)$$

Results are listed in the table:

V_R (m/s)	RCI
12.85	3.94
6.425	3.91
2.57	3.36
1.285	2.27
1.	1.65
0.8764	1.25
0.8180	0.955

A little flurry of excitement developed when it was noted that in the lower part of the table RCI changes markedly with very little difference in V_R . In contrast, in the upper part of the table a minimal change in RCI results from a major increment in V_R . The excitement had two components: First, there is now an understandable reason for the gross overestimate of RCI given by (12), using what had been considered to be the best estimate of V_R . Second, although it is quite apparent now that uncertainties in V_R do not permit us to calculate RCI , perhaps we can turn the problem around and say that over a wide range of reasonable values of RCI (say 0.75 to 1.25), V_R is defined rather narrowly (in this case, near 0.8 m/s). Perhaps this can teach us something about the behavior of hurricanes immersed in a resistant environment, since 0.8 m/s is so much lower than the 13 m/s we calculated by simple vector addition of circulation and translation!

These exciting thoughts quickly evaporated, however, when another source of error was considered: How accurately can direction from the radar to the hurricane center be measured, and what is the effect of an error in this measurement on the calculation of RCI ? During the period when the major component of translational velocity was toward the radar, the measured ratio of shearing to stretching deformation (i.e., b_2 / a_2) was always in excess of a factor of 5. In fact, at our high-quality scan time of 1203 EST, this ratio was 7.5. Reference to (9) shows that a small error of only $\pm 5^\circ$ in estimating hurricane center direction, with b_2 / a_2 initially estimated to be 5, results in error in a_2 of $\begin{Bmatrix} +85\% \\ -88\% \end{Bmatrix}$ but in b_2 of only $\begin{Bmatrix} -5\% \\ +2\% \end{Bmatrix}$. In fact, in our 1203 scan an error in center direction of only -2° would result in an eleven-fold increase in RCI , using (14) and our earlier best estimate of V_R that provide $RCI = 1$, leveraged by terms of opposite sign in (14).

A geometric approach for evaluation of tangential downwind shear was also tried. For most of the observational periods, Doppler velocity values were extracted from the upwind tangential direction [$V_D(270^\circ)$] and the downwind tangential direction [$V_D(90^\circ)$] through the use of a 30° averaging window. In other words, [$V_D(90^\circ)$] is the average of all measurements of Doppler velocity from azimuth angles $\alpha = 75^\circ$ to $\alpha = 105^\circ$. This average was considered a fair estimate, because Doppler velocities generally increased in one azimuthal direction from the tangential axis and decreased in the other direction, owing to the presence of the radial component as well as the curvature and crosswind shear of the tangential component.

Wind vectors important for appreciation of the geometric approach are sketched on Figure 14, which depicts a plan view of a radar (circled - x) conducting a VAD scan of radius r (dotted circle) in the wind field of a cyclone located at a distance R from the radar. Doppler velocities are measured in the tangential upwind [$V_D(270^\circ)$] and downwind [$V_D(90^\circ)$] directions. The tangential and radial components at those azimuth angles are also indicated. Let $\theta = \tan^{-1} r / R$. The angle θ is also the difference in direction of V_T from the radar beam when it is pointing at azimuth angles 90° and 270° . By convention, [$V_D(270^\circ)$] is considered to be negative because it is moving toward the radar, and [$V_D(90^\circ)$] positive because it is moving away. The tangential component of the cyclonic wind field is considered to be positive on both sides of the VAD circle, as it moves cyclonically around the cyclone center; and V_R inflowing toward the center is also positive, by our definition.

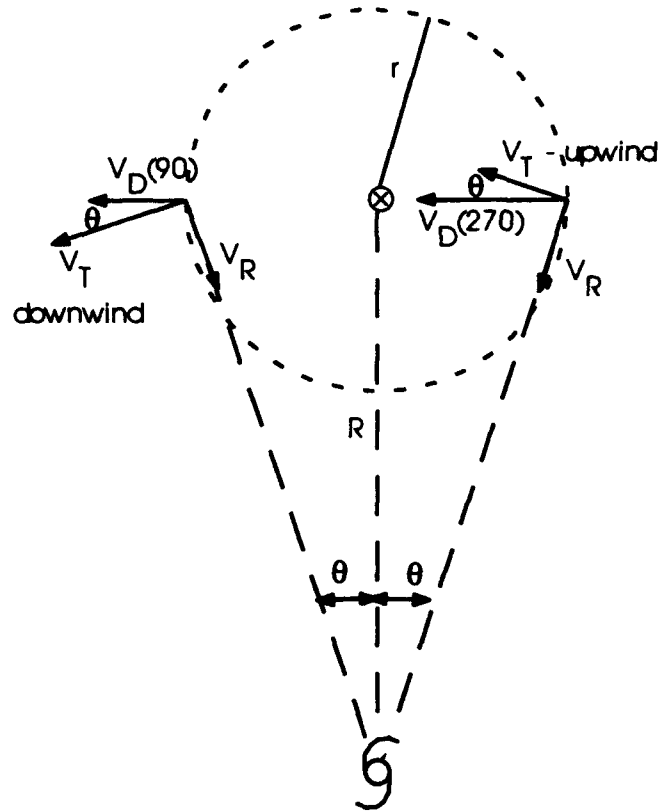


Figure 14. Plan view of radar/ hurricane geometric configuration.

Let us see what contributes to the Doppler velocities:

$$\begin{aligned} V_D(270^\circ) &= -V_T(\text{upwind}) \cos \theta - V_R \sin \theta, \text{ and} \\ V_D(90^\circ) &= V_T(\text{downwind}) \cos \theta - V_R \sin \theta. \end{aligned} \quad (15)$$

Addition of these two expressions yields

$$V_D(90^\circ) + V_D(270^\circ) = \Delta V_T \cos \theta - 2V_R \sin \theta. \quad (16)$$

Since the angle θ is defined as $\tan^{-1} r / R$, $\sin \theta$ is defined as $r / (R^2 + r^2)^{1/2}$ and $\cos \theta$ as $R / (R^2 + r^2)^{1/2}$. Inserting these expressions in (16) and solving for ΔV_T gives

$$\Delta V_T = [V_D(90^\circ) + V_D(270^\circ)] [1 + (r/R)^2]^{1/2} + 2V_R r/R. \quad (17)$$

If we substitute the magnitude of R_C for R in (17), which would be appropriate to the geometry depicted in Figure 14, and insert (17) in (8), we have

$$4rV_R/R_C = a_0 - 2a_2 - [V_D(90^\circ) + V_D(270^\circ)] [1 + (r/R)^2]^{1/2}. \quad (18)$$

As an example, the RCI of our favorite 1203 EST scan, using (18), would be 0.13, clearly very inappropriate for an active hurricane, as Bob most certainly was at this time. However, if we set $RCI = 1$ and solve for V_R , we find $V_R = 1.7$ m/s, far less than the value of nearly 13 m/s we obtained by simple vector addition of circulation (0.2 m/s) and translation (12.7 m/s). This again, as we discovered earlier in the analytic approach, points toward a greatly reduced influence of translation.

These results are qualitatively consistent in 23 of 24 volume scans studied. For example, the seven high-quality scans from 1203 to 1239 EST showed a mean "nominal" radial velocity, given by adding translational components to radar measurements, of 12.1 m/s. However, the mean radial velocity implied by assuming $RCI = 1$ in (18) averaged only 0.4 m/s. In another grouping of high-quality data observed as the hurricane was translating nearly normal to the radar beam (1404 to 1437 EST), the "nominal" radial velocity averaged 2.25 m/s (because very little of the translational velocity was in the radial direction) and the " $RCI = 1$ implied" radial velocity averaged 0.95 m/s. The range of the 1203 - 1239 set averaged 139 km, and averaged 72 km in the 1404 - 1437 set.

Nevertheless, we must remind ourselves anew of the large errors in shearing deformation, and even larger errors in calculation of RCI (or of V_R with the assumption of $RCI = 1$) owing to slight errors in estimating the direction of the hurricane center from

the radar. At 1203 EST the center was 151 km distant, so it might be argued that ordinarily we would be able to locate the center azimuth with an accuracy of better than $\pm 5^\circ$, which at 151 km range amounts to ± 13 km. If so, an error of $+5^\circ$ would imply $V_R = 5.0$ m/s (*inflow*) assuming $RCI = 1$, and -5° error under the same circumstances would imply $V_R = -1.5$ m/s (*outflow*). So even with a sizable error in hurricane center location, we are led toward the conclusion that the translational velocity of the hurricane has considerably less than a simple additive effect on hurricane circulation. However, before we shout this from the rooftops, we might allow for the fact that the mean Doppler velocity readings upwind and downwind may also contribute unknown and possibly significant errors.

In conclusion, two approaches (called analytic and geometric) have been suggested for estimating the tangential downwind shear in a cyclonic circulation as observed by a Doppler radar VAD scan. The tangential downwind shear contributes to the same radar-derived kinematic properties as does the confluence of the radial component of the cyclone circulation. Since we wish to use radial confluence as an independent indicator of the curvature of the tangential component, we regard tangential downwind shear as a contaminant.

Both approaches leave much to be desired, and are rich in uncertainties and error sources. One lesson obvious to this author is the general inapplicability of radial confluence, which may remain effectively obscured except in special circumstances, e.g. in rare cases where stretching deformation is considerably larger in magnitude than shearing deformation, and when the storm translational velocity is mainly normal to the radar beam.

Nevertheless, and despite the frustrating difficulties of this study, two positive results have emerged. One is a deepened appreciation of *PVF* (potential-vortex fit) vis-a-vis *RCI* (radial confluence index). The *PVF* is simple and straightforward to calculate; its potential contaminants in the radial direction are either absent or very small; and in the usual case (as we have observed) with shearing deformation the dominant component of the total deformation, errors owing to imprecise angular location of cyclone center are minimal. In addition, when the radar is in single-station warning mode (e.g., a hurricane approaching a radar), uncertainties are minimized about the effect of translational velocity on the measurement of the tangential component of hurricane circulation. Even in the worst case, when the cyclone moves normal to the radar beam, these uncertainties are not overwhelming, because tangential speeds greatly exceed translational speeds.

The other positive result is the emerging evidence, discussed above, that the hurricane does not simply incorporate translational velocities into its circulation. Our measurements also seem to indicate that rejection of translational velocity by the hurricane circulation is directly range-dependent, which seems reasonable since at some distant outer radius the environment appears to be unaffected by the remote presence of a cyclonic disturbance. Certainly this idea merits continued thought and additional observation, preferably by vector-sensitive means such as dual Doppler measurements.

8.3. VAD Analysis Applied to Hurricane Assessment

The new WSR-88D Doppler radars currently being installed in the United States will offer new opportunities for monitoring the wind field structure of hurricanes. Within the WSR-88D algorithm inventory, there is an algorithm called Velocity Azimuth Display

(VAD). Its primary purpose now is to monitor wind speed and direction as a function of time. In this task, we have explored how the products of this algorithm can be used to monitor hurricanes by looking at these products as a function of time. A detailed presentation of this study is contained in Smalley (1993).

Data collected on August 19, 1991 over a 12 h period by the Phillips Laboratory Doppler radar at Sudbury, MA from Hurricane Bob (1991) were used. The storm approached New England from the south while losing its tropical characteristics. It passed to the east of the radar, with its center being nearest the radar at 1940 UTC. At that time it was at a range of 69 km and an azimuth of 119° .

VAD analyses were performed on selected data during the passage of the storm. Output from these analyses included the zeroth, first, second, and third order harmonic values and the root-mean-square error (RMSE). From this output the horizontal wind speed and direction (from the first order coefficients), divergence (from the zeroth order coefficient), and the stretching and shearing deformations (from the second order coefficients) were determined. Additionally, the magnitudes and azimuthal locations of the 30 degree mean maximum inbound and outbound radial velocities were retrieved along with the azimuthal locations of the two zero isodops for each VAD scan. These data were analyzed in height and time to determine the evolution of the wind field of the hurricane.

8.3.1. VAD-Derived Wind Parameters

The VAD scheme was used to compute the horizontal wind speed and direction from the first order coefficients. It was found that the horizontal wind direction veered with height, while at a given altitude the direction backed with time. Figure 15 is a contoured depiction of the vertical profile of the horizontal wind direction over the analysis time period. At the start of the time period (with the hurricane about 125 km

due south of the radar) the winds veered with height in the layer from northeast to east. With time, the winds backed at all levels, resulting in an enhancement of the northerly component throughout the layer. At the end of the time period (with the hurricane about 100 km slightly north of east of the radar) the wind direction veered with height through the layer from north-northwest to north.

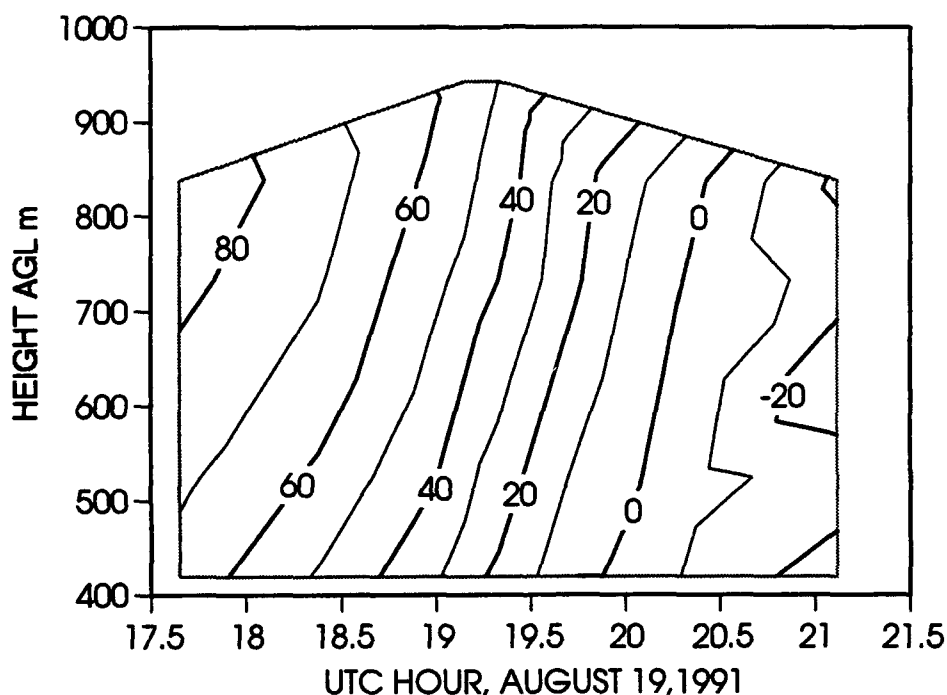


Figure 15. Contours of wind direction estimates as a function of height and time.

A similar examination of the horizontal wind speed revealed a steady increase with time for all levels, peaking at around 2020 UTC in the middle of the analysis layer. Fig. 16 is a contoured depiction of the vertical profile of the horizontal wind speed over the analysis time period. Interestingly, the peak (from the north) occurs with the hurricane virtually due east of the radar. The maximum wind speed in the layer was centered at about 600 m AGL. This altitude of maximum wind speed is consistent with that found in other hurricanes (Burpee, 1986). Reduction of the wind speed lower in the

layer is due in part to surface frictional effects. The change in wind direction from east-northeast to north with time is consistent with the translation of tight cyclonic flow to the east of the radar.

While we get very useful insight from the wind speeds and directions derived from VADs, there is much more information in these analyses. For example, in the technical report (Smalley, 1993), we present other wind field parameters and show how these are indicative of storm behavior. Parameters examined include

- zero isodop azimuthal separation (diffuence indicator)
- azimuthal separation between upstream and downstream velocity peaks
- shearing deformation

Each of these parameters displayed a characteristic pattern, namely an abrupt change around 1900 GMT. As an example, Fig. 8-5 shows the azimuthal separation of the zero isodop in the vertical for each time. This figure along with those for the other parameters give us insight into the behavior of the hurricane as it approaches. The full discussion of these analyses is given in Smalley (1992).

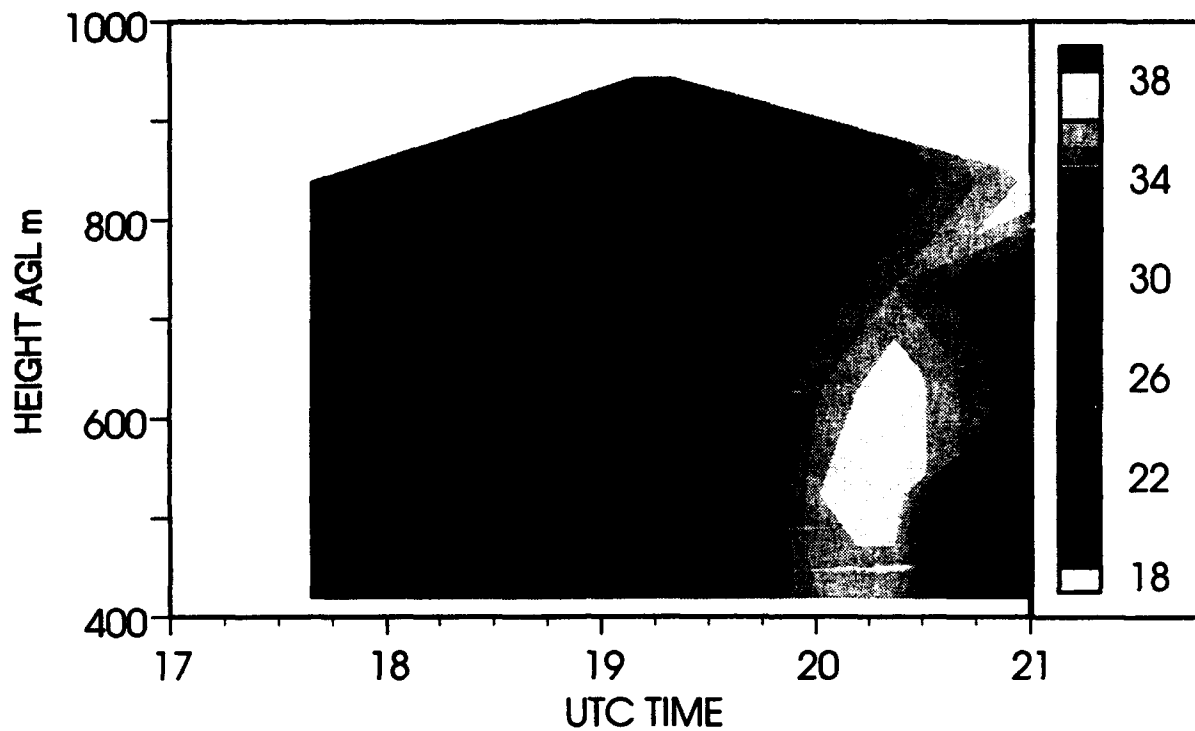


Figure 16. Contours of wind speed estimates as a function of height and time.

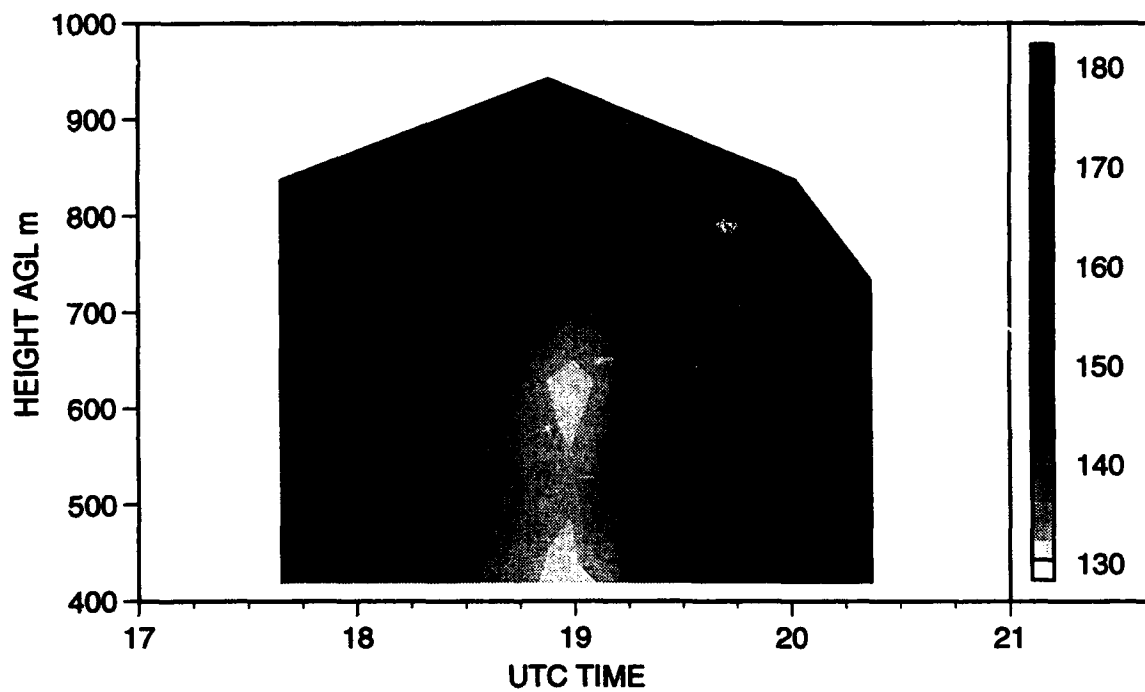


Figure 17: Vertical Profiles of zero isodop azimuthal separation vs. height above ground level. Each profile is identified by its time tag (UTC).

8.3.2. VAD Perturbation Wind Field

Besides looking at parameters derived from VAD analyses, we also examined the residual fields that result from a subtraction of the VAD derived wind field (up to the second harmonic) from the Doppler velocities. For a given elevation angle, VAD analyses were performed at regular range intervals. From the coefficients derived from these analyses, a radial velocity field was computed as a function of azimuth and range. This computed radial velocity field was then subtracted from the measurements, leaving a residual or perturbation field. We then examined this residual field for any organization that could be related to any structure seen in the reflectivity factor fields.

The velocity perturbations were found to be correlated with radar reflectivity gradient regions. A possible mechanism to explain these relationships would be that within this weak reflectivity regime small convective cells exist. These cells would have a slightly higher reflectivity than their surroundings and associated inflow and outflow regions within the overall deteriorating hurricane circulation. These mesoscale regions perturb the mean hurricane flow and are observed as radial velocity perturbations from the least-squares-fit VADs. Because of the weakness of the structure in both the reflectivity and velocity fields, it is not possible to draw any definitive conclusions from this aspect of the study. However, this approach could be quite useful in other situations.

8.3.3. Conclusions

This effort has extended the use of the VAD to the hurricane situation as a diagnostic tool. In particular, we showed that

- a) VAD-derived horizontal wind speed and direction can be used as an alternative to reconnaissance aircraft flight level winds,

b) shearing deformation and horizontal wind speed can be used as indicators of hurricane proximity,

c) a combination of the above parameters, zero-isodop azimuthal separation, and azimuth of the inbound V_{rad} maximum can be used as trend indicators of the hurricane's proximity and tropical nature,

d) VAD-calculated radial velocity perturbation patterns are related to embedded convective cells within the reflectivity field or possibly to disruption of hurricane circulation

e) cross-azimuthal V_{rad} contours allows the assessment of vertical shear of the horizontal wind regimes of the hurricane and ambient environments.

Future research in these areas, particularly with data from more representative and vigorous hurricanes, has the potential of refining the ability of using VADs as an analysis and diagnostic tool for hurricanes.

9. Wind Profiler Evaluation

9.1. Introduction

A study to assess the performance of a Wind Profiler Doppler radar was conducted at the Ground-based Remote Sensing Branch of the US. Air Force's Phillips Laboratory at Maynard, Massachusetts. The purpose of this study is to determine the usefulness of the Wind Profiler in providing wind data of sufficient accuracy and resolution necessary for such operations as missile launch support. There are two aspects to this effort: the development of a database for the PL wind profiler data, Loran sonde data, and all ancillary data and the evaluation of the profiler performance. Both of these efforts are documented in separate reports (Smalley, 1992; Smalley, 1993).

A Loran radiosonde (sonde) system was developed at Phillips Laboratory as the reference standard to determine the accuracy of the profiler-measured winds. In comparison with reference standard radars at Wallops Island, VA the sonde was found to have a vector accuracy of 0.32 m s^{-1} (Morrissey, 1992). The Wind Profiler was manufactured by Paramax as part of NOAA's Wind Profiler Demonstration Network. Its principles of operation are described by van de Kamp (1988). Briefly, the wind profiler measures the radial velocity component of the wind field via a vertical beam and two horizontally orthogonal, off-vertical beams in a low (0.5-9.25 km) and high (7.5-16.25 km) mode. These radial velocities are combined to yield the horizontal wind.

The premise of this study is to characterize the observed differences in the measured wind fields of the sondes and the wind profiler to assess the latter's capability to provide data sufficient for Air Force needs. The sonde system as noted above was selected as the reference standard for this comparison. There are a number of sources

for the errors in the observed wind differences in this experiment other than those due to the accuracy limitations of each sensor:

- a) time differences of the wind measurements of the sensors,
- b) the separation distance of the wind measurements of the sensors,
- c) small scale fluctuations in the wind field and the response of each sensor to them.

9.2. Study Description

For this study, 117 sondes were launched from a mobile platform in east central Massachusetts between January 1991 and April 1992. Typically, one of three launching schemes was followed: 1) successive launches from a single site on a launch day, 2) dual launches synchronized from dual sites, and 3) dual launches from a single site. The study was set up so each sonde passed by the profiler at some point during its flight. The majority of the launches originated between 15-30 km upstream (west) of the profiler site.

An anticyclonic flow regime was well established over the monitoring region on virtually all the launch days. Therefore, consideration for concerns such as precipitation dominance of the returned profiler signal, the inhibition of the sonde's ascent due to precipitation accretion, or non-homogeneity of the wind field across the profiler beams due to rigorous convection are not necessary.

Since this study has been outlined in detail in a recent technical report, we will only summarize its results here. The wind profiler operated 24 hours/day during the study. Therefore, wind data were measured somewhat concurrently by the sonde and profiler. However, there is not perfect temporal or spatial correspondence between the profiler and Loransonde estimates. The sonde derived wind estimates are averages over finite line segments along the balloon path, with each estimate having a unique time associated. On the other hand, the profiler estimates consist of the combination of components derived from one minute averages of measurements. For the latter case, the component averages are not coincident in either space or time, but are derived successively along three separate beams.

An analysis of wind profiler data and sonde data was performed to assess the ability of the profiler to provide winds of an accuracy and resolution necessary for Air Force needs. The two independent data sets were combined for this analysis into a common format modeled after the gate spacing of the profiler data. Mean and variance values of the profiler and sonde wind components, the component differences, and other pertinent parameters were computed for each gate (72 total) for each of the three profiler temporal resolutions. Additionally, these data were grouped and analyzed in 4.25 km vertical slices of the atmosphere.

Beyond the inaccuracies associated with each of the measuring techniques there also are spatial and temporal contributors to the observed error. These spatial and temporal contributors are not easily separated from each other. For this report an initial analysis was undertaken to better understand some of these relationships between time and space. Some interesting results arise that merit further analysis.

The mean gate component errors between the 60 minute profiler data and the sondes were small, generally, less than 0.5 m s^{-1} for the U-component and less than 1.0 m s^{-1} for the V-component. This was observed for both the low mode and high mode of the data. The standard deviations for the component errors for the low mode gates ranged between $1.5\text{-}2.5 \text{ m s}^{-1}$. The range was about $2.5\text{-}3.5 \text{ m s}^{-1}$ for the high mode gates. For both modes, the mean component error and standard deviation increase slightly with increasing gate height. Recall that the vector accuracy of the sonde was found to be 0.32 m s^{-1} . If the Air Force requirement specifies a 1.0 m s^{-1} accuracy of the wind vector, the observed means and standard deviations for the components do not ensure that the wind profiler can provide this accuracy, particularly for the high mode.

In the 7.5-9.25 km overlap region, the better agreement of the spatial sampling of the sensors for the low mode results in less error than for the high mode. When the sonde data were smoothed so that there was closer spatial agreement, the high mode gate mean component errors were reduced, but not significantly. This indicates that most of the small scale variability in the component error is attributable to the small scale fluctuations in the sonde data since these occur on scales not resolved in the profiler data, especially the 60 minute data.

The gain in temporal resolution when using the profiler's 12 or 6 minute data is outweighed by the lack of any quality control on these data. Thus, there is at least an order of magnitude increase in the mean component errors for these resolutions with respect to the 60 minute data. This is especially true above 4-5 km altitude in the low mode. A negative bias of the V-component errors and a positive bias of the U-component errors were noted to be independent of profiler data resolution.

The mode analysis also yielded pertinent results. No relationship between component error and profiler-sonde separation distance was found. This holds for either mode and any of the three profiler temporal resolutions. This was expected to be a source of error found by this analysis. Since this expectation is not substantiated in our analysis, the sources of the mean component error are more likely to be linked to the subtleties of the spatial (horizontal and vertical) and temporal relationships between the wind field and the sensors. A relationship may exist, but was not found in this study for two reasons. First, the experimental design promoted sonde passages close to the profiler. Second, since the observed region above the planetary boundary layer has a quasi-geostrophic flow, the large scale flow field is less variable and it is possible that the separation distances were too short to resolve it.

Another result of the mode analysis is similar to that found in the gate-to-gate analysis. There is a negative bias to the V-component error and a positive bias to the U-component error. This bias is independent of profiler data resolution and is most pronounced in the middle tropospheric layers. That is, the bias was observed in the top half of the low mode and the bottom half of the high mode (this includes the overlap region). This requires further analysis.

A relationship between component error and vertical velocity (VV) was discovered in the mode analysis of the 6 minute profiler data. For cases of vertical velocity greater than absolute 0.5 m s^{-1} , it was found that a best fit line of slope -2.25 describes the VV to U-component error situation, and a slope of 4.47 describes the VV to V-component error relationship. This shows that there is a distinct relationship between poor 6 minute profiler wind data and high vertical velocities. For the 6 minute resolution these data can be problematic, but for the 60 minute data the consensus check effectively eliminates this problem.

An analysis of the shear measured by these sensors was also performed. Good agreement was found in magnitude and trend of the mean gate-to-gate low mode shear measured by both sensors. In the high mode, there is a larger disparity. This, undoubtedly, goes back to the spatial resolution discrepancy (the sonde data are not smoothed). With all the low mode data grouped together, it was found that the 60 minute resolution profiler measured shear ($\Delta z = 500$ m) was about 60% of that measured by the sonde. This percentage was similar for the comparison of the shear vector's components also. The results for the high mode, with the larger spatial sampling discrepancy, were not nearly so well correlated.

Certainly, further analysis is needed and this data set would be valuable as such. Presently, the observed component errors can not be completely resolved. Only a small amount of the error is attributable to the sonde itself or to the separation distance between the sonde and profiler. We have not been able to distinguish the how much of the remaining error is attributable to the profiler and to spatial/temporal perturbations. Thus, it can not be concluded that the 1 m s^{-1} Air Force criterion for errors can be met by the wind profiler. The curious bias in the component errors also needs further analysis.

10. References

- Bals, T. M., 1991: Precipitation mapping. STX Scientific Report #2, PL-TR-91-2033, ADA246724.
- Barclay, and Wilk, 1970: Severe thunderstorm radar echo motion and related weather events hazardous to aviation operations. ESSA Technical Memo., ERLTM-NSSL 46, 63 pp.
- Bohne, A. R. and F. I. Harris, 1985: Short term forecasting of cloud and precipitation. AFGL-TR-85-0343, AD A169744.
- Bohne, A. R., F. I. Harris, P. A. Sadoski and D. Egerton, 1988: Short term forecasting of cloud and precipitation. AFGL-TR-88-0032, 94 pp, ADA212692.
- Burpee, R.W., 1986: Mesoscale structure of hurricanes. (Chapter 14 in Mesoscale Meteorology and Forecasting, Ray, P.S., ed., *Amer. Met. Soc.*, Boston, MA, 311-331 pp.
- Donaldson, R.J., Jr., 1991: A proposed technique for diagnosis by radar of hurricane structure. *J. Appl. Meteor.*, 30, 1636-1645.
- Endlich, R. M. and D. E. Wolf, 1981: Automatic cloud tracking applied to GOES and METEOSAT observations. *J. Appl. Meteor.*, 20, 309-319.
- Freeman, H., 1961: On the encoding of arbitrary geometric configurations. *IRE Trans. Electron. Comput.*, EC-10, 260-269.

Hamann, D. J., 1991: Front detection with Doppler radar. STX Scientific Report, #3, PL-TR-91-2034, ADA242880.

Hamann, D. J., 1992: Wind discontinuity detection. HSTX Scientific Report, in press.

Harris, F. I., and D. Smalley, 1993: Detection of precipitation phase and freezing rain. HSTX Scientific Report, in press.

Morrissey, J., 1992: Wind Measurement Accuracy of a Loran Radiosonde System. PL-TR-92-2262, ADA263572

Smalley, 1992: A performance assessment of a wind profiler Doppler radar. HSTX Scientific Report, in press.

Smalley, 1993: On the extension of the VAD Technique as a tool in hurricane analysis. HSTX Scientific Report, in press.

van de Kamp, D., 1988: PROFILER TRAINING MANUAL #1 Principles of Wind Profiler Operation. NOAA/ERL, Boulder, CO. 49 pp.

Wood, V. T. and R. A. Brown, 1987: Simulated land-based NEXRAD Doppler measurements within hurricanes. Preprints, 17th Conf. on Hurricane and Tropical Meteorology, Amer. Meteor. Soc., 174-177.

Zittel, W. D., 1976: Computer applications and techniques for storm, tracking and warning. Preprints, 17th Conf. on Radar Meteor., 514-521.